Gain-of-function mutation of microRNA-140 in human skeletal dysplasia

HHS Public Access
Author manuscript
Nat Med. Author manuscript; available in PMC 2019 August 25.

Published in final edited form as:
Nat Med. 2019 April ; 25(4): 583–590. doi:10.1038/s41591-019-0353-2.

Gain-of-function mutation of microRNA-140 in human skeletal dysplasia

Giedre Grigelioniene[1,2,3,15], **Hiroshi I. Suzuki**[4,15], **Fulya Taylan**[2], **Fatemeh Mirzamohammadi**[1], **Zvi U. Borochowitz**[5], **Ugur M. Ayturk**[6], **Shay Tzur**[7,8], **Eva Horemuzova**[9,10], **Anna Lindstrand**[2,3], **Mary Ann Weis**[11], **Gintautas Grigelionis**[2], **Anna Hammarsjö**[2,3], **Elin Marsk**[12], **Ann Nordgren**[2,3], **Magnus Nordenskjöld**[2,3], **David R. Eyre**[11], **Matthew L. Warman**[6], **Gen Nishimura**[13], **Phillip A. Sharp**[4,14], and **Tatsuya Kobayashi**[1,*]

[1]Endocrine Unit, Massachusetts General Hospital and Harvard Medical School, Boston, Massachusetts, USA

[2]Department of Molecular Medicine and Surgery and Center for Molecular Medicine, Karolinska Institutet, Stockholm, Sweden

[3]Department of Clinical Genetics, Karolinska University Hospital, Stockholm, Sweden

[4]David H. Koch Institute for Integrative Cancer Research, Massachusetts Institute of Technology, Cambridge, Massachusetts, USA

[5]Rappaport Faculty of Medicine, Technion – Israeli Institute of Technology; Medical Genetics Clinics, Assuta Medical Center, Haifa, Israel

[6]Orthopaedic Research Labs, Department of Orthopaedic Surgery, Boston Children's Hospital, Boston, Massachusetts, USA

[7]Laboratory of Molecular Medicine, Rambam Health Care Campus, Haifa, Israel

[8]Genomic Research Department, Emedgene Technologies, Tel Aviv, Israel

[9]Department for Women's and Children's Health, Karolinska Institutet, Stockholm, Sweden

[10]Pediatric Endocrinology Unit, Karolinska University Hospital, Stockholm, Sweden

[11]Department of Orthopedics and Sports Medicine, University of Washington, Seattle, Washington, USA

[12]Department of Otorhinolaryngology, Karolinska University Hospital, Stockholm, Sweden

[13]Intractable Disease Center, Saitama University Hospital, Saitama, Japan

*Correspondence to: tkobayashi1@mgh.harvard.edu, Tatsuya Kobayashi, MD, PhD, Endocrine Unit, Massachusetts General Hospital, 50 Blossom Street. Boston, Massachusetts 02114, USA.
[15]These authors contributed equally: Giedre Grigelioniene, Hiroshi I. Suzuki.

Author Contributions

G. Grigelioniene, H.I.S., and T.K. designed the study and wrote the manuscript. G. Grigelioniene, H.I.S., T.K., F.T., F.M., U.M.A., S.T., A.L., M.A.W., G. Grigelionis, A.H., D.R.E., M.L.W., and P.A.S. conducted experiments and data collection. E.M., A.N., M.N., G.N., Z.U.B., and E.H. performed clinical characterization. All authors contributed to data interpretation and revised the manuscript.

Competing Financial Interests

S.T. works at Emedgene Technologies, and P.A.S. is a board member of Syros Pharmaceuticals.

[14]Department of Biology, Massachusetts Institute of Technology, Cambridge, Massachusetts, USA

Abstract

MicroRNAs (miRNAs) are posttranscriptional regulators of gene expression. Heterozygous loss-of-function point mutations of miRNA genes are associated with several human congenital disorders[1–5], but neomorphic (gain-of-new-function) mutations in miRNAs due to nucleotide substitutions have not been reported. Here we describe a neomorphic seed region mutation in the chondrocyte-specific, super-enhancer-associated *MIR140* encoding microRNA-140 (miR-140) in a novel autosomal dominant human skeletal dysplasia. Mice with the corresponding single nucleotide substitution show skeletal abnormalities similar to those of the patients but distinct from those of miR-140-null mice[6]. This mutant miRNA gene yields abundant mutant miR-140-5p expression without miRNA-processing defects. In chondrocytes, the mutation causes widespread derepression of wild-type miR-140-5p targets and repression of mutant miR-140-5p targets, indicating that the mutation produces both loss-of-function and gain-of-function effects. Furthermore, the mutant miR-140-5p seed competes with the conserved RNA-binding protein Ybx1 for overlapping binding sites. This finding may explain the potent target repression and robust *in vivo* effect by this mutant miRNA even in the absence of evolutionary selection of miRNA-target RNA interactions, which contributes to the strong regulatory effects of conserved miRNAs[7,8]. Our study presents the first case of a pathogenic gain-of-function miRNA mutation and provides molecular insight into neomorphic actions of emerging and/or mutant miRNAs.

Genetic skeletal disorders comprise a large group of approximately 500 clinically distinct and genetically heterogeneous conditions. Mutations in approximately 400 different genes are currently known to cause congenital skeletal diseases[9], but underlying molecular mechanisms are not elucidated for many of them. Herein, we describe a novel skeletal dysplasia caused by a single nucleotide substitution in the *MIR140* gene and the underlying mechanism.

A novel skeletal dysplasia was identified in two unrelated families in a project for molecular diagnosis of ultra-rare congenital skeletal disorders (Fig. 1a, b). In Family 1, individual II-2, patient 1, P1, is affected, as is one of her sons (III-2, P2). In Family 2, II-1, P3, is the only affected individual. Clinical features of the skeletal dysplasia included disproportionate short stature with short limbs, small hands and feet, and midface hypoplasia with small nose. The radiological hallmarks were mild spondylar dysplasia, delayed epiphyseal ossification of the hip and knee, and severe brachydactyly with cone shaped phalangeal epiphyses (Fig. 1c–p, and auxology data in Supplementary Table 1). The spondylar and epiphyseal abnormalities evolved into premature spondylosis and degenerative joint disease in adulthood, respectively. P1 and P2 also suffered from frequent respiratory infections with prolonged cough and inspiratory stridor. P1 had a narrow larynx likely due to floppy cartilage (Extended Data Fig. 1a–c). All three affected individuals had normal intelligence, dentition, hearing, visual acuity, and basic blood tests.

Whole genome sequencing (WGS) identified the same heterozygous nucleotide substitution (chr16:g.69967007A>G (hg19), *MIR140*:NR_029681.1:n.24A>G) in P1 and P2 (Fig. 1a, q,

Extended Data Fig. 1d, and Online Methods). The same single nucleotide substitution occurred *de novo* in P1 and P3, and co-segregated with the skeletal dysplasia phenotype in Family 1 (Fig. 1a and Extended Data Fig. 1d). In P3, since the phenotype was recognized as this novel clinical diagnostic entity, it was first detected by Sanger sequencing and then confirmed retrospectively in the exome sequencing and WGS data (Extended Data Fig. 1d). This substitution is located at the first nucleotide of the seed sequence of the highly conserved microRNA (miRNA), miR-140-5p, encoded by *MIR140* (Fig. 1q, r and Extended Data Fig. 1e), and is not reported in the gnomAD, a large scale human genome sequence database[10]. *MIR140* is associated with a chondrocyte-specific super-enhancer both in humans and mice (Fig. 1s and Extended Data Fig. 2), consistent with this miRNA's high expression in chondrocytes. Super-enhancers commonly drive high-level expression of tissue-specific genes, including miRNA genes, with evolutionarily conserved cell type-specific function[11–13].

miR-140-5p and miR-140-3p (collectively miR-140) are abundantly and relatively specifically expressed in chondrocytes[14,15], and loss of miR-140, encoded by *Mir140*, in mice leads to short stature and craniofacial abnormalities[6,16]. This miR-140-null phenotype included mildly advanced terminal differentiation of growth plate chondrocytes of developing bones[6,17]. To investigate the possible disease-causing role of the mutant miR-140, we introduced this single-nucleotide substitution into the mouse genome using the CRISPR-Cas9 technology[18]. We then compared the skeletal phenotype of heterozygous (miR-140$^{G/+}$) and homozygous (miR-140$^{G/G}$) knock-in mice with those of wild-type (miR-140$^{+/+}$) and the previously reported knockout (miR-140$^{-/-}$) mice (Supplementary Table 2)[6].

Although miR-140$^{G/G}$ and miR-140$^{-/-}$ mice were smaller and had shorter noses than wild-type littermates (Fig. 2a, b and Extended Data Fig. 3a), only miR-140$^{G/G}$ and miR-140$^{G/+}$ mice showed delayed secondary ossification of tubular and carpal bones (Fig. 2c–f), decreased expression of *Col10a1*, a maturation marker for hypertrophic chondrocytes (Extended Data Fig. 3b), and delayed cartilage maturation of the larynx, trachea, and anterior ribs (Extended Data Fig. 3c, d). Micro-CT analysis showed severely decreased epiphyseal mineralization in miR-140$^{G/G}$ mice (Fig 2g). The proliferation rate of tibial growth plate chondrocytes was not significantly different among miR-140$^{G/G}$, miR-140$^{G/+}$, and wild-type mice (Extended Data Fig. 3e). We did not find an increased number of apoptotic cells in the growth plate of miR-140$^{G/G}$ mice (Extended Data Fig. 3f). miR-140$^{G/G}$ and miR-140$^{G/+}$ mice showed mildly flat vertebral bodies (Extended Data Fig. 3g). The basal skull growth plate was wider due to the increased length of all layers of chondrocytes in miR-140$^{G/G}$ and miR-140$^{G/+}$ mice, whereas miR-140$^{-/-}$ mice showed no significant changes (Fig. 2h). The proximal tibial growth plate also showed an expansion of the resting zone in miR-140$^{G/G}$ and miR-140$^{G/+}$ mice (Extended Data Fig. 3h). These bone abnormalities of miR-140$^{G/G}$ and miR-140$^{G/+}$ mice are consistent at all analyzed ages from P7 to P56 when compared to wild-type mice (Supplementary Table 2) and are highly consistent with the skeletal dysplasia features of the patients, presenting with delayed secondary ossification, mild platyspondyly, small epiphyses, and scaphocephaly. Taken together, these differences in phenotype between miR-140$^{G/G}$ and miR-140$^{-/-}$ mice, and delayed epiphyseal maturation in humans, indicate that this single-base substitution causes a

neomorphic, and not just loss-of-function, effect. Furthermore, the delayed skeletal maturation observed in humans and mice with the miR-140 substitution suggests a common pathogenic mechanism.

Small RNA sequencing analysis in mouse chondrocytes revealed that the miR-140 A>G mutation yields slightly greater amounts of the mutant miR-140-5p (miR-140-5p-G) than wild-type miR-140-5p, while decreasing two miR-140-3p species (3p.1 and 3p.2) (Fig. 3a, Extended Data Fig. 4a–c, and Supplementary Table 3). Minor changes in Dicer processing sites and miRNA strand choice were also observed (Extended Data Fig. 4d, e); this finding is consistent with the critical role of the 5′-end structure of pre-miRNAs and miRNA duplexes in Dicer processing and in asymmetric miRNA strand selection[19,20]. These data indicate that the A>G mutation did not compromise miRNA processing and yielded abundant expression of miR-140-5p-G from primary miR-140 transcripts of which transcription is strongly activated by a super-enhancer in chondrocytes.

Since miRNAs have global impacts on target mRNA expression, we next investigated transcriptome effects of the miR-140 mutation. Principle component analysis and hierarchical clustering analysis of the RNA-seq data clearly distinguished miR-140$^{G/G}$ and miR-140$^{G/+}$ mice from miR-140$^{-/-}$ and wild-type mice (Fig. 3b, c). Expression levels of genes within the neighborhood of the miR-140 gene locus were not largely affected (Extended Data Fig. 5a). We predicted potential *de novo* targets of miR140-5p-G using the TargetScan (v7.0/1)[21] (Extended Data Fig. 5b and Supplementary Tables 4 and 5). Target sites of miR-140-5p-G seldom overlapped with those of wild-type miR-140 species (wild-type 5p, 3p.1, and 3p.2) and were less conserved than those of wild-type miR-140 species (Extended Data Fig. 5c–e). Both the miR-140 A>G mutation and miR-140 deletion caused derepression of conserved 8mer target genes for wild-type miR-140-5p and to a lesser extent for miR-140-3p species (Fig. 3d and Extended Data Fig. 6a), suggesting that miR-140-5p exerts greater target repression than miR-140-3p even though the latter is more abundant. Importantly, the widespread suppression of predicted miR-140-5p-G targets is only observed in miR-140$^{G/G}$ and miR-140$^{G/+}$ chondrocytes (Fig. 3d and Extended Data Fig. 6a). This suppressive effect of miR-140-5p-G is particularly strong for 8mer target sites (Extended Data Fig. 6b) and correlates with the predicted miRNA target efficiency (Extended Data Fig. 6c), suggesting that the miR-140-5p-G-target interaction follows the molecular rules of conventional miRNA targeting. Accordingly, wild-type and the mutant miR-140-5p showed similar target site efficiencies by TargetScan prediction (Extended Data Fig. 6d). A 3′ UTR reporter assay, using minimal target sequences and endogenous 3′ UTR sequences, confirmed that miR-140-5p-G and wild-type miR-140-5p target their respective predicted 8mer target sites with similar strengths, and validated the efficiency of target sites in several genes, respectively (Fig. 3e, f and Supplementary Table 6).

The miR-140-5p-G targets include many genes important for skeletal development and homeostasis, including *Loxl3, Btg1*, and *Trps1*, and genes associated with various metabolic pathways (Fig. 3g and Supplementary Table 7)[22–24]. Furthermore, gene set enrichment analysis (GSEA) revealed that the hypoxia pathway is impaired in miR-140$^{G/G}$, but not in miR-140$^{-/-}$ chondrocytes (Fig. 3h, i)[25,26]. The coding region of *Hif1a* that encodes a master transcription factor controlling hypoxic response[27] contains a conserved sequence

complementary to the miR-140-5p-G seed sequence. Hif1a protein expression was reduced in miR-140$^{G/G}$ chondrocytes (Extended Data Fig. 7a). Along with the mutation experiment of the target site (Extended Data Fig. 7b), this suggests that miR-140-G directly suppresses *Hif1a*. Consistent with these findings, mRNA expression of Hif1a and Hif1a-regulated molecules including lysyl oxidases, essential for collagen crosslinking, significantly decreased in miR-140$^{G/G}$ chondrocytes, with a concomitant decrease in collagen crosslinking in the rib cartilage (Fig. 3j and Extended Data Fig. 7c–e). These alterations in genes important for cartilage and chondrocyte functions may contribute to the skeletal abnormalities of miR-140$^{G/G}$ and miR-140$^{G/+}$ mice. In addition, expression of several extracellular matrix genes including *Col10a1* decreased in miR-140$^{G/G}$ and miR-140$^{G/+}$ chondrocytes (Extended Data Fig. 7f), as confirmed by *in situ* hybridization analysis for *Col10a1* (Extended Data Fig. 3b).

Gene regulation by conserved miRNAs has a significant impact on 3′ UTR evolution, and evolutionarily maintained target sites mediate actions of miRNAs more effectively than non-conserved target sites[28]. In light of this miRNA-target coevolution concept[7,8], an intriguing question is how “newly emerged” miR-140-5p-G exerts such potent target repression and robust *in vivo* effects. Since a mutation in the miRNA seed region creates a new repertoire of target genes and the magnitude of such target suppression is typically small, a neomorphic mutant miRNA would need to target a biologically important regulatory network in order to produce a disease phenotype. Because the seed sequence of the mutant miR-140-5p-G is not shared with other known miRNAs and multiple RNA binding proteins (RBPs) are reported to modulate miRNA function[29], we hypothesized that miR-140-5p-G conversely interferes with conserved RBP pathways. Computational analysis suggested that the miR-140-5p-G seed in the Ago2 complex and the RBP, Ybx1 (also known as YB-1), potentially compete for the same RNA binding sites (Fig. 4a and Extended Data Fig. 8a)[30–32]. This hypothesis is supported by the binding of YBX1 to several miR-140-5p-G target genes in a previously reported YBX1 individual nucleotide resolution crosslinking and immunoprecipitation (iCLIP) dataset (Extended Data Fig. 8b)[32]. YBX1 is a multifunctional RBP that stabilizes mRNAs and regulates RNA splicing[33,34]. We performed single-end enhanced CLIP (seCLIP) analysis of Ybx1 and Ago2, a central component of the miRNA pathway, in wild-type and miR-140$^{G/G}$ chondrocytes to test this hypothesis (Extended Data Fig. 8c–e)[35,36]. Ago2 seCLIP analysis revealed crosslink site-centric enrichment of hexamer sequences complementary to the seed sequences of wild-type miR-140-5p and miR-140-5p-G in Ago2 seCLIP clusters in wild-type and miR-140$^{G/G}$ chondrocytes, respectively (Fig. 4b, c and Extended Data Fig. 9a, b). Accordingly, genes with the identified 3′ UTR target sites of miR-140-5p-G were downregulated only in miR-140$^{G/G}$ and miR-140$^{G/+}$ chondrocytes, while genes with wild-type miR-140-5p target sites were upregulated in both miR-140-null and miR-140 mutant chondrocytes (Fig. 4d). This effect was not apparent for the target sites in coding sequences (CDS) (Extended Data Fig. 9c). Next, Ybx1 seCLIP analysis identified a binding motif similar to the Ybx1 binding motif reported previously[30–32] (Fig. 4e). It also demonstrated crosslink site-centric enrichment of a hexamer sequence (“ACCACC”) complementary to the seed of miR-140-5p-G (Fig. 4f and Extended Data Fig. 10a, b). Analysis of Ybx1 seCLIP signals at the seCLIP clusters identified in wild-type chondrocytes showed that the miR-140 mutation preferentially attenuated seCLIP signals at the 3′ UTR

sites with the ACCACC hexamer among the representative Ybx1 target sequences, CAUC/CACC hexamers (Fig. 4g). This trend was not observed for the CDS seCLIP clusters (Fig. 4g), suggesting a predominant competition between miR-140-5pG and Ybx1 in 3′ UTRs. Importantly, miR-140-5p-G Ago2 seCLIP target genes with Ybx1 binding in the 3′ UTR showed stronger repression in mutant chondrocytes than those without Ybx1 binding (Fig. 4h). Furthermore, a single-cell 3′ UTR reporter assay of several miR-140-5p-G target genes demonstrated that suppressive effects by miR-140-5p-G were dampened by Ybx1 inhibition (Fig. 4i and Extended Data Fig. 10c, d). In addition, previously reported YBX1-stabilized transcripts were preferentially repressed in miR-140$^{G/G}$ and miR-140$^{G/+}$ chondrocytes as compared with miR-140$^{-/-}$ chondrocytes (Extended Data Fig. 10e)[34]. Furthermore, systematic RBP motif analysis suggested that Ybx1 activity was selectively suppressed in miR-140$^{G/G}$ but not in miR-140$^{-/-}$ chondrocytes (Extended Data Fig. 10f, g). These observations collectively suggest that the potent suppressive effect of miR-140-5p-G is partly attributable to the competition against Ybx1, especially in 3′ UTRs, and subsequent suppression of Ybx1 activity.

Besides gene dosage abnormalities[37,38], single nucleotide substitutions in two miRNA genes have been identified in human diseases: *MIR96* mutations in autosomal dominant deafness 50 (#613704) and *MIR184* mutations in EDICT syndrome (#614303) and familial and sporadic cases of keratoconus[1–5,39]. However, these mutations, occurring at multiple different nucleotides of single miRNAs, are thought to primarily cause loss of function (Supplementary Table 8). In contrast, the miR-140 mutation found in this study affected the same nucleotide in both families and resulted in gain of a new function as well as loss of the original function, as shown by the transcriptome analysis revealing repression of new target genes and derepression of original targets. Although it is unusual that a “newly emerged” miRNA exerts such a potent biological effect, in this instance, the disease phenotype may be at least partially explained by potential competition with the RBP, Ybx1, and by the super-enhancer-driven high-level miRNA expression (Fig. 4j). This finding suggests that sequence-dependent crosstalks with RBPs may confer extended biological properties to miRNAs and other types of regulatory RNAs. Such sequence-dependent competition between a miRNA seed and an RBP would add a new mechanism of transcript regulation. Our subsequent systematic analysis of siRNA off-target data and genome-scale RNAi-based loss-of-function screens for essential genes in cancer cells has recently confirmed and reinforced this concept (crosstalk with endogenous RBPs; ceRBP) in general[40]. We observed that ceRBP effects are widespread in RNAi and contributes to off-target effects and phenotype modulation[40]. Therefore, avoiding RBP binding motif overlap with seed sequences may further minimize RNAi off-target effects.

Overall, the present study expands our knowledge on how mutations in miRNAs contribute to human disease development and thus suggests the possibility that some of currently unresolved congenital disorders may be caused by neomorphic miRNA mutations. In addition, given the expansion of miRNA genes in vertebrates[7,8], the molecular mechanism revealed in this present study also has broader implications in understanding how function of new miRNA genes might evolve in humans.

Methods

Ethical approvals

The study was approved by the Ethics Committee of the Karolinska Institutet (2014/983-31/1, 2012/2106-31/4) and Israel Research Board no. 0072-13-BNZ. Animal studies were approved by the Institutional Animal Care and Use Committee (IACUC) of the Massachusetts General Hospital (2009N000217). Written informed consent for research participants was obtained from the patients and from the parents of the involved minors. P1 (currently 45 years old) has kindly provided her childhood photo for publication and the authors have obtained signed proof of informed consent. The patients were examined at the Karolinska University Hospital, Stockholm, Sweden [Family 1, Patients 1 and 2 (P1, P2)] and at the Assuta Medical Center, Haifa, Israel [Family 2, Patient 3 (P3)] due to unknown ultra-rare skeletal dysplasia.

Clinical diagnosis of spondyloepiphyseal dysplasia (SED) MIR140 type Nishimura

One of the authors (G.N.) recognized radiographic similarities between the unrelated individuals, diagnosed the disorder in the first family (P1 and P2) as a novel skeletal dysplasia, and then diagnosed P3 as having the same disorder. Because the phenotype has not been reported previously and these patients were found to have the same variant in the *MIR140* gene, we propose the eponym of spondyloepiphyseal dysplasia (SED) MIR140 type Nishimura. The present disorder should be differentiated from acrodysostosis. Both disorders share several features, including midface hypoplasia and brachydactyly with cone-shaped epiphyses. However, epiphyseal maturation is delayed in SED MIR140 type Nishimura, whereas epiphyseal ossification, particularly carpal ossification, is advanced in acrodysostosis. In addition, epiphyseal dysplasia, a hallmark in SED MIR140 type Nishimura, is not a feature in acrodysostosis. Furthermore, the presented patients did not have mutations in the *PDE4D* and *PRKAR1A* genes known to be associated with acrodysostosis. They did not show any of endocrine abnormalities seen in acrodysostosis such as hypocalcemia, hyperphosphatemia, elevated levels of parathyroid hormone (PTH) and/or thyroid stimulating hormone (TSH), and decreased insulin-like growth factor 1 (IGF-1). P1 had measurement of bone density by Dual-energy X-ray absorptiometry at the age of 43. She had normal bone density for the age, which suggests that the heterozygous *MIR140* mutation in humans does not lead to bone mass abnormalities.

Identification of the *MIR140* mutation

Exome sequencing analysis (ES) was initially performed for both families in quartet for Family 1 (the proband, P1, her unaffected parents, and her affected son, P2) and in trio for Family 2 (the proband, P3, and her unaffected parents). Since the disease was inherited in an autosomal dominant way in Family 1, we searched for *de novo* variants in P1. For Family 2, ES was initially performed independently from Family 1, searching for *de novo* or autosomal recessively inherited mutations. No potential disease causing variants were found in the protein coding genes.

Next, whole genome sequencing (WGS) was performed, searching for variants in both protein coding and protein non-coding genes for Family 1 in quartet. A single nucleotide

substitution in chr16: 69967007 A>G in the *MIR140* gene (+24A>G) in P1 (II-2) and her affected son P2 (III-2) was detected and confirmed by Sanger sequencing (Fig. 1q and Extended Data Fig. 1d). This single nucleotide substitution occurred *de novo* in P1 and was transmitted to her son. This variant segregated with the skeletal dysplasia phenotype in Family 1. The same *de novo* single nucleotide substitution was detected using Sanger sequencing in P3, and the mutation was retrospectively confirmed in exome sequencing data of Family 2 (Extended Data Fig. 1d).

Screening P1, P2, and P3 for possible disease causing variants in 378 known skeletal dysplasia genes using WGS data, and screening P2 for gene dose abnormalities of the above mentioned skeletal dysplasia genes using custom-designed comparative genome hybridization analysis was all negative (data not shown), excluding involvement of these genes in the skeletal dysplasia phenotype of our patients.

An extended search in copy number variation (CNV) databases regarding human phenotypes associated with CNVs involving the *MIR140* gene revealed a single individual with heterozygous 1.1Mb deletion with isolated Arnold-Chiari malformation[41]. No individuals with short stature and heterozygous deletions of greater than 2Mb size including the *MIR140* gene were reported in the CNV databases (https://decipher.sanger.ac.uk/). This result suggests that haploinsufficiency of *MIR140* does not lead to skeletal abnormalities in humans, consistent with the normal phenotype previously reported in heterozygous miR-140 knockout mice[6], supporting the hypothesis that the heterozygous nucleotide substitution (chr16:g.69967007A>G (hg19), *MIR140*:NR_029681.1:n.24A>G) is a neomorphic mutation.

Clinical data

The information regarding the symptoms and features was collected from the patient records. The skeletal dysplasia was identified as unique by expert pediatric radiologist (G.N.) in the first family and recognized by the same radiologist in the second patient. In auxology analysis, the z-scores at birth and at follow up were calculated using the Swedish growth reference data[42] and WHO auxology calculator (http://www.childgrowthcalculator.com/).

The DNA extraction and analyses

DNA was extracted from the peripheral venous blood samples (2-10 ml) from the patients and their family members. For DNA extraction from the samples of Family 1, we used the Qiagen Puregen Blood Core kit C (Qiagen). Phenol-chloroform DNA extraction protocol was applied for DNA extraction from the members of Family 2.

The following methods were applied for DNA examination of family 1: whole exome and whole genome sequencing for I-1, I-2, II-2, and III-2, comparative genomic hybridization-array for III-2, and Sanger sequencing of *MIR140* for all family members; and for family 2: whole exome sequencing for I-1, I-2, and II-1, whole genome sequencing for II-1, and Sanger sequencing for *MIR140* for all family members.

Exome Sequencing (ES)

Libraries for sequencing on Illumina HiSeq2500 (Illumina Inc) were prepared from genomic DNA. Exome sequences were enriched with the Agilent SureSelect XT All Exon V5 target enrichment kit (Agilent Technologies), according to manufacturers' instructions. On average, this resulted in >64 million mapped unique sequences with a mean coverage of 135, *i.e.*, 10x coverage for 97.9% of target sequences. Post-capture libraries were sequenced as 2×101 bp paired-end reads, which were base-called using CASAVA (bcl2Fastq v1.8.3, Illumina Inc). For bioinformatic analysis, the following steps were performed as described previously[43]. Reads were mapped to the human reference genome (hg19) using MOSAIK (2.2.3). Duplicates were marked with Picard 1.92. Variants were called using the Genome Analysis Tool (GATK v.3.2.0), annotated using both ANNOVAR (version 2014 July 14) and Variant Effect Predictor (VEP), and loaded into the GEMINI (v0.16.0) database. Variants that were rare with Minor Allele Frequency less than 1% in 1000 Genomes Project (2014 Oct version) all populations, 6500 NHLBI-GO Exome Sequencing Project (EVS) and Exome Aggregation Consortium (ExAC v0.2)[10] were considered for further analysis. dbSNP138 nonflagged was used to annotate known SNPs. Combined Annotation Dependent Depletion (CADD) was used to score the deleteriousness of single nucleotide variants (SNVs).

Whole genome sequencing (WGS)

Libraries for sequencing on Illumina HiSeqX Ten (Illumina Inc) were prepared from the genomic DNA using the Illumina TruSeq PCR-free kit with a mean insert size of >350 bp. On average, this resulted in >620 million mapped unique sequences with a mean coverage of >29, *i.e.*, 19x coverage for 80% of reference sequences. An in-house pipeline developed by Science For Life Laboratory, Stockholm, Sweden was used to map reads to the human reference genome (hg19). Data were aligned to the reference genome using bwa (v0.7.12)[44]. The raw alignments were then deduplicated, recalibrated, and cleaned using GATK (v3.3-0-geee94ec)[45]. The quality control information was gathered using Qualimap (v2.0)[46]. SNVs and indels were called using the HaplotypeCaller in GATK. The variants were further analyzed using the following steps as described previously[43]. The variants were processed with GenotypeGVCFs, VariantRecalibrator, ApplyRecalibration, and SelectVariants tools in GATK, then functionally annotated using Variant Effect Predictor (VEP), and loaded into a database using GEMINI (v0.16.0). The variants were explored in the database using built-in tools in GEMINI.

Comparative genomic hybridization (CGH) array

CNV screening using a custom-designed exon targeted array. Comparative genomic hybridization (CGH) was performed using the DNA sample of P2 targeting 872 genes involved in skeletal dysplasias, ciliary disorders and malformation syndromes (Agilent Technologies). The custom array design was created using e-Array (https://earray.chem.agilent.com/earray/), Agilent's online resource for custom array design. Briefly, we used a 2×4000k array format to create a design with an average coverage of one probe per 100 bp in coding sequences and one probe per 500 bp in non-coding sequences in the target genes and at the same time to retain a genome-wide background resolution of 50 kb

across the genome. Experiments were performed according to the manufacturer's recommendation with minor modifications

as described previously[47]. The copy number data analysis was performed using the Agilent Genomic Workbench software (Agilent Technologies).

PCR, Sanger sequencing, and genotyping

To confirm the WGS and ES findings, we used PCR primers: MIR140F 5′-CCGTGGATGGATGTTCCTTTTT-3′ and MIR140R 5′-GGCTTGAGCTAAACCAGCAAG-3′ to amplify and sequence the *MIR140* gene. The primers were used to amplify 281bp fragments of the *MIR140* locus of the genomic DNA from the patients and their family members. The obtained PCR products were purified with ExoSAP-IT (Thermo Fisher Scientific) and sequenced at the MGH DNA core facility.

Mice

The animal study was approved by the Institutional Animal Care and Use Committee of the Massachusetts General Hospital and performed in accordance with the regulations and guidelines. miR-140-null mice were previously described[6]. For generation of knock-in mice with the A>G substitution in the *Mir140* gene, we used *in vivo* CRISPR-Cas9 editing in mouse zygotes according to an established protocol[48]. Wild-type Cas9 mRNA, a guide RNA with the Cas9 handle, and a single-stranded oligomer DNA repair template were injected into one-cell stage C57/B6 mouse embryos. The sequence of the guide RNA is 5′-CATAGGGTAAAACCACTGGC-3′. For the repair template, a 140 base-long single-stranded oligomer DNA with the A>G single nucleotide substitution (corresponding to the mutation) at the 70th nucleotide from the 5′-end was synthesized. This substitution creates a novel restriction enzyme site (*Msp* I; CCGG). Founder mice were screened by PCR followed by *Msp* I digestion. For genotyping, a 216-nt genomic sequence containing the mutation site was amplified using the PCR primers, Mir140-F 5′-TCTGTGTTCATCCCATCCTG-3′ and Mir140-R 5′-ATGGAGTCCTTCGATGCAGA-3′ and digested with *Msp* I. The PCR amplicon containing the A>G substitution is digested into 98 bp and 119 bp long fragments. Out of 61 mice embryos injected with the guide RNA, repair template and Cas9, 11 mice were positive for the knock-in mutation. Among them, 5 mice were selected for further characterization of the genomic modification. All of these mice were compound heterozygous with one allele mutated as desired and the other with various size insertion-deletion mutations. After confirming the absence of additional mutations in the 2 kb region surrounding the *Mir140* gene using Sanger sequencing, we selected two founder lines, crossed them to wild-type C57/B6 mice to breed out the opposite allele to generate heterozygous F1 lines (miR-140$^{G/+}$). F1 lines were further intercrossed to generate homozygous mutants (miR-140$^{G/G}$). The consistency of the phenotype was confirmed in two lines. The sample size was estimated based on our prior experience of performing similar sets of experiments and the number of examined mice is shown in Supplemental Table 2.

Skeletal preparation and histology

For the skeletal examination, one side of extremities were taken for whole-mount-staining with alizarin red with or without alcian blue staining, and the contralateral extremities were fixed in formalin, decalcified, embedded in paraffin, sectioned, and stained with hematoxilin-eosin (H/E) or safranin O for microscopic examination for 1 , 2, 3, 4, and 8 week-old mice. The number of examined mice is summarized in Supplemental Table 2. Tibias of 14 day-old mice and skulls of 4 week-old animals were examined by micro-CT analysis to determine the formation of the secondary ossification and details in skull anatomy. For two week-old animals, bones were also stained with alizarin red. The growth plate in the basal skull of 7 day-old mice was sectioned, stained with hematoxylin-eosin according to the standard protocol, and histologically examined. Since we found no phenotypic differences between males and females, males and females were not discriminated for the analysis. Lengths of the growth plate and its zones were measured using the image processor, Fiji. Lengths of total and different zones of tibial growth plates at P56 were also measured. Tibia growth plates are irregular, thus the measurements were performed by selecting a rectangle area in the middle flattest part of each growth plate section, averaging the height of each zone in the middle and at the edges. The trachea and larynx of 56 day-old animals were examined by whole-mount staining followed by histological analysis.

Primary rib chondrocyte culture

Primary rib chondrocytes were isolated from the frontal part of the rib cage of 7-day-old mice. Muscle, soft tissues, and mineralized rib and sternal bones were removed using fine tweezers and surgical scissors under a dissection microscope. Dissected costal cartilage rods were then incubated in a digestion medium containing Dulbecco modified Eagle medium (DMEM), 10% fetal calf serum (FCS), and 0.2% (approximately 600 U/ml) collagenase type II (Worthington) at 37 °C for 6 hours. Cells were released from the cartilage matrix by gentle pipetting, passed through nylon mesh strainers (BD Falcon), spun to remove collagenase, counted, plated at the concentration of 1×10^5 cells/ml in the DMEM medium containing 10% FCS and cultured overnight.

Total RNA, including microRNAs, was isolated using the Direct-zol RNA MiniPrep kit (Zymo Research). For Western blot analysis, cells were lysed in 2x Laemmli sample buffer. Proteins were resolved in 4 – 20% gradient acrylamide/MOPS gels, transferred on nitrocellulose membrane and incubated with indicated antibodies (anti-Hif-1a antibody (NB100-449) from Novus Biologicals, anti-beta actin antibody (#4970S) and anti-Ybx1 antibody (#9744S) from Cell Signaling Technology). Uncropped blots are shown in Source Data.

BrdU labeling and detection

For BrdU labeling, 50 μg of BrdU per gram of body weight was given to mice intraperitoneally 2 hours before sacrifice. Tissues were fixed in 10% formalin solution, processed, and sectioned using standard procedures. BrdU was detected using the BrdU-staining kit (Life Sciences). The BrdU-labeling index was calculated as the ratio of BrdU-positive nuclei over total nuclei in a standardized region of the growth plate.

TUNEL staining

Apoptosis was evaluated in proximal tibial growth plates of 7 day-old miR-140$^{G/G}$ and miR-140$^{+/+}$ mice using the *In Situ* Cell Detection Kit (Sigma Aldrich) according to the manufacturer's protocol.

Micro-CT analysis

Assessment of the bone morphology and microarchitecture was performed by high-resolution micro–computed tomography (mCT40; Scanco Medical) as previously described[49]. In brief, the proximal tibial epiphysis and metaphysis were scanned using the condition of 70 kVp peak X-ray tube potential, 113 mAs X-ray tube current, 200 ms integration time, and 10-mm isotropic voxel size. For the epiphysis, the total mineralized tissue volume was evaluated. Cancellous bone was assessed in the proximal tibial metaphysis. The epiphysis and primary spongiosa were identified by semi-manual contouring of the regions of interest. Micro-CT analysis was performed in a blinded manner with all mice assigned to coded sample numbers.

Collagen crosslink analysis

Costal rib cartilage was isolated from 4 week-old mice. Cartilage was scraped clean, defatted with chloroform/methanol (3:1 v/v), hydrolyzed in 6N HCl, dried, dissolved in 1% (v/v) n-heptafluorobutyric acid and analyzed by C18 reverse-phase HPLC as described[50]. Lysylpyridinoline (LP) and hydroxylysylpyridinoline (HP) were quantified. Statistical analysis was performed using one-way ANOVA and *post hoc* Tukey-Kramer test.

Super-enhancer analysis

Four H3K27Ac ChIP-seq datasets in human chondrocytes (donor id 57: GSM916058, GSM1112777, donor id 58: GSM1112794, GSM772791, donor id 59: GSM1112787, GSM670044, donor id 60: GSM1112786, GSM772781) were derived from the ENCODE project. Human datasets were aligned to the version hg19 of the human genome. Mouse H3K27Ac and Sox9 ChIP-seq profiles were previously described[51]. Mouse datasets were aligned to the version mm9 of the mouse genome using bowtie 1.0.1[52] with the following parameters: -n 2, -e 70, -m 1, -k 1. Identification of ChIP-seq peaks were performed using MACS 1.4.2.[53] with parameters -p 1e-9, –keep-dup = auto, -w –S –space = 50, and -g hs (or mm). We used ROSE (https://bitbucket.org/young_computation/rose) for identification of super-enhancers according to previous reports[12,13]. A stitching distance and a TSS exclusion zone size were set to 12500 bp and 2500 bp, respectively.

RNA sequencing and analysis

Libraries were prepared using the Illumina TruSeq Stranded mRNA sample preparation kit from 500 ng of purified total RNA according to the manufacturer's protocol, and sequenced on Illumina NextSeq500. Single-end 75bp sequences were read. Sequenced reads were aligned to the mm9 reference genome assembly and gene counts were quantified using STAR (v2.5.1b)[54] and Cufflinks (2.2.0)[55]. In Extended Data Fig. 7f, the reads were mapped to the mouse genome with RNA-seq Unified Mapper (RUM), and gene expression changes was calculated in R by the counting and normalization of uniquely mapped reads and by

using edgeR[56,57]. For differential expression (Extended Data Fig. 7d and 7f), statistical analysis was performed using one-way ANOVA and *post hoc* Tukey-Kramer test.

Small RNA sequencing and analysis

Total RNA was extracted from chondrocytes using the Direct-zol RNA MiniPrep kit (Zymo Research). Small RNA libraries were constructed with the NEBNext Small RNA Library Prep Set for Illumina (New England Biolabs) and analyzed by Illumina HiSeq 2000. Obtained sequences were processed for adaptor removal and size exclusion of sequences < 15 nt with Cutadapt. Filtered reads were mapped to the mm9 genome assembly with bowtie 1.0.1, allowing two mismatches, and further quantitated using miRBase v21 as previously described[52,58]. Drosha and Dicer cleavage sites were inferred from the 5′-ends of 5p and 3p miRNAs, respectively. Selection of a single mature miRNA strand from miRNA duplex is determined by combination of 5′-end nucleotide identity and thermodynamic asymmetry of miRNA duplex termini[20]. Ago2 prefers strands with 5′-uridine or 5′-adenosine and thermodynamically unstable 5′-ends. This mechanistically explains abundant expression of miR-140-3p compared with miR-140-5p in chondrocytes. Prediction of the 5p/3p ratio of WT and mutant miRNA duplexes was performed using 5′-trinucleotide sequences according to our previous report[20]. The A>G substitution is predicted to destabilize the 5′-end of the 5p arm and thus to increase the 5p/3p ratio for both 5p/3p.1 and 5p/3p.2 duplexes, consistent with the increase in miR-140-5p and decrease in miR-140-3p in chondrocytes from miR-140G/+ and miR-140G/G mice. Sequence analysis of miR-140 is summarized in Supplementary Table 3.

Target identification of miR-140-5p-G and bioinformatics

Identification of miR-140-5p-G was performed using stand-alone computation pipelines of the latest version of TargetScan (v7.0)[21] released in September of 2016. We performed target predictions for both mouse and human 3′ UTR annotations and analyzed target site conservation and cumulative weighted context++ score (CWCS) using TargetScanMouse and TargetScanHuman, respectively. We used TargetScanMouse predictions for subsequent analyses. These predictions are included in Supplementary Tables 4 and 5. Datasets of target genes of all miRNAs were downloaded from the TargetScan database (v7.1; targetscan.org) in September of 2016. After filtering out genes with a maximum count across all samples less than 1, normalized FPKM (Fragments Per Kilobase of transcript per Million) data were used for subsequent analyses. For target gene expression changes, P values were calculated by one-sided Kolmogorov–Smirnov (K-S) test for either direction: upregulation or downregulation. GO analysis was carried out using Database for Annotation, Visualization, and Integrated Discovery (DAVID; https://david.abcc.ncifcrf.gov).

Gene set enrichment analysis and RBP motif analysis

Gene set enrichment analysis (GSEA) was performed with the GSEA software (http://software.broadinstitute.org/gsea/index.jsp) using C2CGP gene set collections[25]. Enrichment map analysis was further applied for GSEA results[26]. In Fig. 3h, enrichments in WT vs. miR-140$^{G/G}$ and WT vs. miR-140-null cells are mapped to the node borders and inner node area, respectively. Red and blue represent upregulation and downregulation in WT cells relative to miR-140$^{G/G}$ or miR-140-null cells, respectively. Node size represents the number

of genes overlapped. For motif analysis in Fig. 4a and Extended Data Fig. 8a, we performed RNA binding protein motif analysis using the CISBP-RNA database (http://cisbp-rna.ccbr.utoronto.ca/index.php)[30]. As for Ybx1 binding motif, RNAcompete, SELEX, and human iCLIP data in glioblastoma cells were previous described[30–32]. In Extended Data Fig. 10e, YBX1 target gene analysis was performed using GSE63562 datasets[34]. We selected genes downregulated by YBX1 knockdown ($P < 0.05$, $FC > 2$) in MDA-MB-231 cells as YBX1-regulated genes and used for subsequent analysis. To perform systematic RBP motif analysis, we collected mouse representative 3′ UTR sequences of all genes from TargetScanMouse (v7.1) and predicted all possible bindings sites of 94 human/mouse RBPs using RBPmap (http://rbpmap.technion.ac.il/) and a high stringency option[59]. For each gene, RBP target score (RTS) for each RBP was calculated as follows: RTS = Σ (Z score of each binding site). Then, for each RBP, genes with top 200 RTS were considered as strong possible RBP targets and used as a gene set in GSEA in Extended Data Fig. 10f, g.

qRT-PCR analysis

qRT-PCR was performed on cDNA synthesized by the Verso cDNA Synthesis Kit (Thermo Fisher Scientific) using EvaGreen qPCR Supermix (Solis Biodyne). Primer sequences are described in Supplementary Table 9. Statistical analysis was performed using one-way ANOVA and *post hoc* Tukey-Kramer test.

Plasmids

A pri-miRNA expression vector was prepared by inserting short fragments of pri-miR-140 into pcDNA6.2-GW/EmGFP-miR (Thermo Fisher Scientific) as previously described[20]. 3′ UTR reporter vectors were generated by inserting miRNA target site sequences or 3′ UTRs of miR-140-5p-G target genes into the 3′ UTR of the luciferase gene in the psiCHECK-2 dual luciferase reporter vector (Promega). For the Hif1a CDS expression plasmid, a Flag-tagged mouse Hif1a cDNA was cloned into the pcDNA3 vector. The 3′ UTR sequences of mouse *Btg1*, *Ehd1*, *Trps1*, and *Loxl3* were inserted into the 3′ UTR of mCherry in the bidirectional pTRE-Tight-BI (Clontech) eYFP and mCherry reporter vector. Mutations were introduced by a PCR-based approach. Primer sequences are given in Supplementary Table 9.

Luciferase reporter assay

HEK293T cells were obtained from American Type Culture Collection and cultured in a Dulbecco's Modified Eagle's Medium (Thermo Fisher Scientific) supplemented with 10% fetal bovine serum (FBS), penicillin, and streptomycin. HEK293T cells are tested for mycoplasma contamination. Cells were transfected with luciferase reporter and pri-miRNA expression plasmids using TransIT-LT1 (Mirus). Cell extracts were collected 48 hours after transfection. The ratio between firefly and *Renilla* luciferase was determined using Dual-Luciferase Reporter Assay System (Promega). We independently repeated the molecular biology experiment at least twice, and all attempts to reproduce the results were successful. The sample size was estimated based on our prior experience of similar sets of experiments.

Hif1a target site analysis

48 hours after transfection with Flag-Hif1a and pri-miRNA expression plasmids, HEK293T cells were lysed with a buffer containing 1% Nonidet P-40, 20 mM Tris-HCl, pH 7.4, 150 mM NaCl, 5 mM EDTA, and cOmplete™, Mini, EDTA-free Protease Inhibitor Cocktail Tablet (Sigma) and subjected to Western blot analysis using anti–Flag M2 (F1804, Sigma) and anti–α-tubulin DM-1A (T9026, Sigma) antibodies. Uncropped blots are shown in Source Data.

seCLIP analysis

seCLIP were performed in mouse wild-type and mutant primary chondrocytes using Ago2 and Ybx1 antibodies, as previously described[35,36]. Anti-Ago2 antibody (2D4), and anti-Ybx1 antibody (D2A11, #9744S) were from Wako and Cell Signaling Technology, respectively. seCLIP libraries were analyzed by Illumina HiSeq 2000. Identification of seCLIP clusters enriched against size-matched input (SMinput) was performed as previously described[35]. First, obtained sequences were processed for adaptor removal, and reads mapped to repetitive elements were removed. Remaining reads were aligned to the mm9 reference genome assembly using STAR (v2.5.1b), and seCLIP clusters for IP samples were identified using the CLIPper peak calling algorithm (https://github.com/yeolab/eclip) with the following parameters: --bonferrroni --superlocal --threshold binomial. Finally, peak normalization vs SMinput was performed, and enriched seCLIP clusters were extracted. Hexamer enrichment analysis was performed using the 40nt sequences flanking the center of seCLIP clusters on both directions, all possible hexamers, and background sequence sets generated by HOMER (v4.10)[60]. In Fig. 4b, 4c, and 4f, non-intronic seCLIP clusters were analyzed, since enrichment of miRNA motifs and Ybx1 motifs was not observed in intronic clusters (Extended Data Fig. 9b and 10b) and majority of intronic clusters was considered to be non-specific due to the low sensitivity of seCLIP for small starting materials like primary chondrocytes. In. Fig. 4e, motif prediction was performed using all Ybx1 seCLIP clusters in wild-type chondrocytes, the 20nt sequences flanking the center of seCLIP clusters on both directions, and HOMER. In Fig. 4g, the seCLIP site coverage was calculated using the window of seCLIP cluster regions and 20nt extension on both directions.

Single-cell dual fluorescence reporter assay

HEK293T cells were first transfected with control or YBX1 siRNA (Dharmacon, siGENOME SMARTpool siRNA) using Lipofectamine RNAiMAX (Thermo Fisher Scientific). 24 hr later, eYFP and mCherry reporter, rtTA expression vector, and pri-miRNA expression plasmids were subsequently cotransfected using TransIT-LT1 (Mirus). 4 hr after the second transfection, HEK293T cells were treated with 1 μg/ml doxycycline (Sigma). 48 hr after the second transfection, flow cytometry analysis was carried out with BD FACS Celesta (BD Biosciences). Data collection was performed using FACS Diva Version 8.0.1. FlowJo version 10.4.1. and R was used for data analysis. After selection of single cell populations by sequential gating by SSC and FSC (Extended Data Fig. 10d), we analyzed about 20,000 eYFP-positive cells (P3 population in Extended Data Fig. 10d). Each experiment included non-transfection controls. The eYFP and mCherry signals of each cell were background normalized by subtracting the mean value plus two standard deviation of

signal in non-transfected samples, and binned by eYFP signal levels, as previously described[40].

Statistical analysis

Sample sizes were determined based on our prior experience of performing similar sets of experiments. The number of examined mice is shown in Supplemental Table 2. Statistical tests were performed using R (3.5.0). In Fig. 2g, 2h, and Extended Data Fig. 3h, differences among multiple groups were analyzed using Kruskal-Wallis one-way ANOVA and *post hoc* Steel-Dwass test. In Fig. 3a, 3e, 3f and Extended Data Fig. 3a, 7c, 7d, 7e, and 7f, statistical analysis was performed using one-way or two-way ANOVA and *post hoc* Tukey-Kramer test. In Fig. 3d, 4d, and 4h, and Extended Data Fig. 6a, 6b, 9c, and 10e, P values were calculated by one-sided Kolmogorov–Smirnov (K-S) test for either direction: upregulation (U) or downregulation (D). For K-S test, Bonferroni correction was performed in Fig. 3d, 4d, and 4h, and Extended Data Fig. 6a, 6b, and 9c. In Fig. 4b, 4c, and 4f, and Extended Data Fig. 9a and 10a, statistical significance was assessed using two-sided Fisher's exact test with Bonferroni correction. In Extended Data Fig. 9b and 10b, statistical significance was assessed with one-sided Fisher's exact test with Bonferroni correction. In Fig. 4g, statistical significance was assessed with two-sided Wilcoxon rank sum test with Bonferroni correction. In molecular biology experiments, results are representative of more than two independent and reproducible experiments. In all bar graphs, data are expressed as mean ± s.e.m. In all box plots, center lines show medians; box limits indicate the twenty-fifth and seventy-fifth percentiles; whiskers extend to 1.5× the interquartile range.

Life Sciences Reporting Summary

Further information on experimental design is available in the Life Sciences Reporting Summary.

Data Availability

Data generated during this study are available in the Gene Expression Omnibus under accession number GSE98309. The human variant is deposited in the ClinVar database (SCV000586692.1). Human genome data from the individuals participating in the study is protected by Swedish law (2006:351), and raw Sanger sequencing data within the area of interest is available upon request. All other data will be made available upon request to the corresponding author.

Extended Data

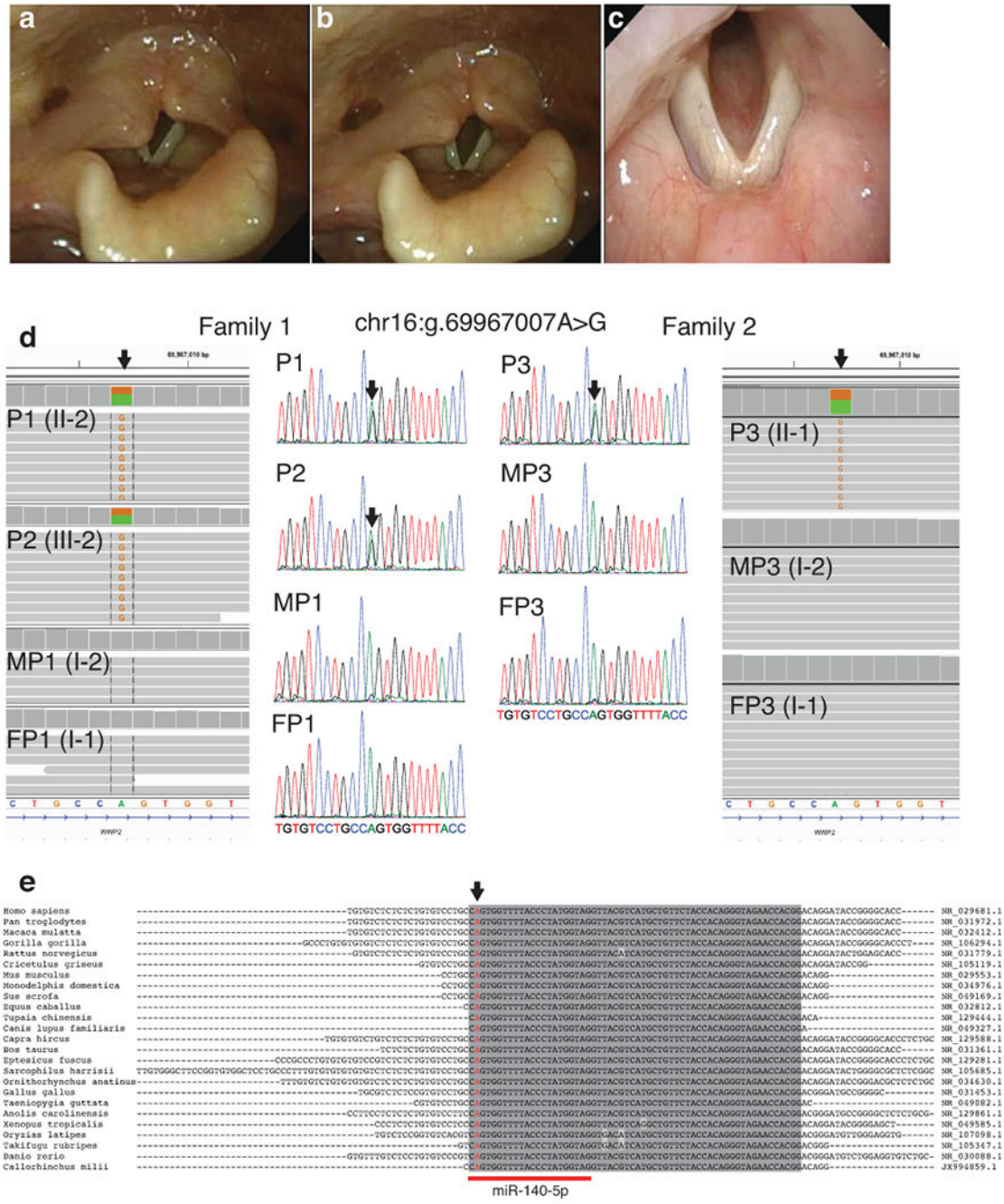

Extended Data Figure. 1. Human phenotype and genotype.

a-c, Fiberscopy findings in P1, 44 years of age, consistent with laryngomalacia. The right arytenoid cartilage is enlarged with redundant soft tissues and it prolapses antero-medially over the larynx during inspiration (**a**). Reduced laryngeal contraction is observed during expiration (**b**). A close view of the larynx and vocal folds shows dorsal narrowing of the subglottic region (**c**).

d, The pathogenic variant in *MIR140* (chr16:g.69967007A>G) (indicated by black arrows) in whole genome sequencing and exome sequencing data (left and right panels), and its

Sanger sequencing confirmation (middle panel) in individuals P1, 2, and 3 as in Fig. 1. Position of the mutation is according to GRCh37 (hg19). MP1 = mother of P1, FP1 = father of P1, MP3 = mother of P3, and FP3 = father of P3.

e, Evolutionarily conservation of *MIR140* in different species; miRNA hairpin sequence is highlighted in grey. The second nucleotide in miR-140-5p is conserved from human to Australian ghostshark (indicated by a black arrow).

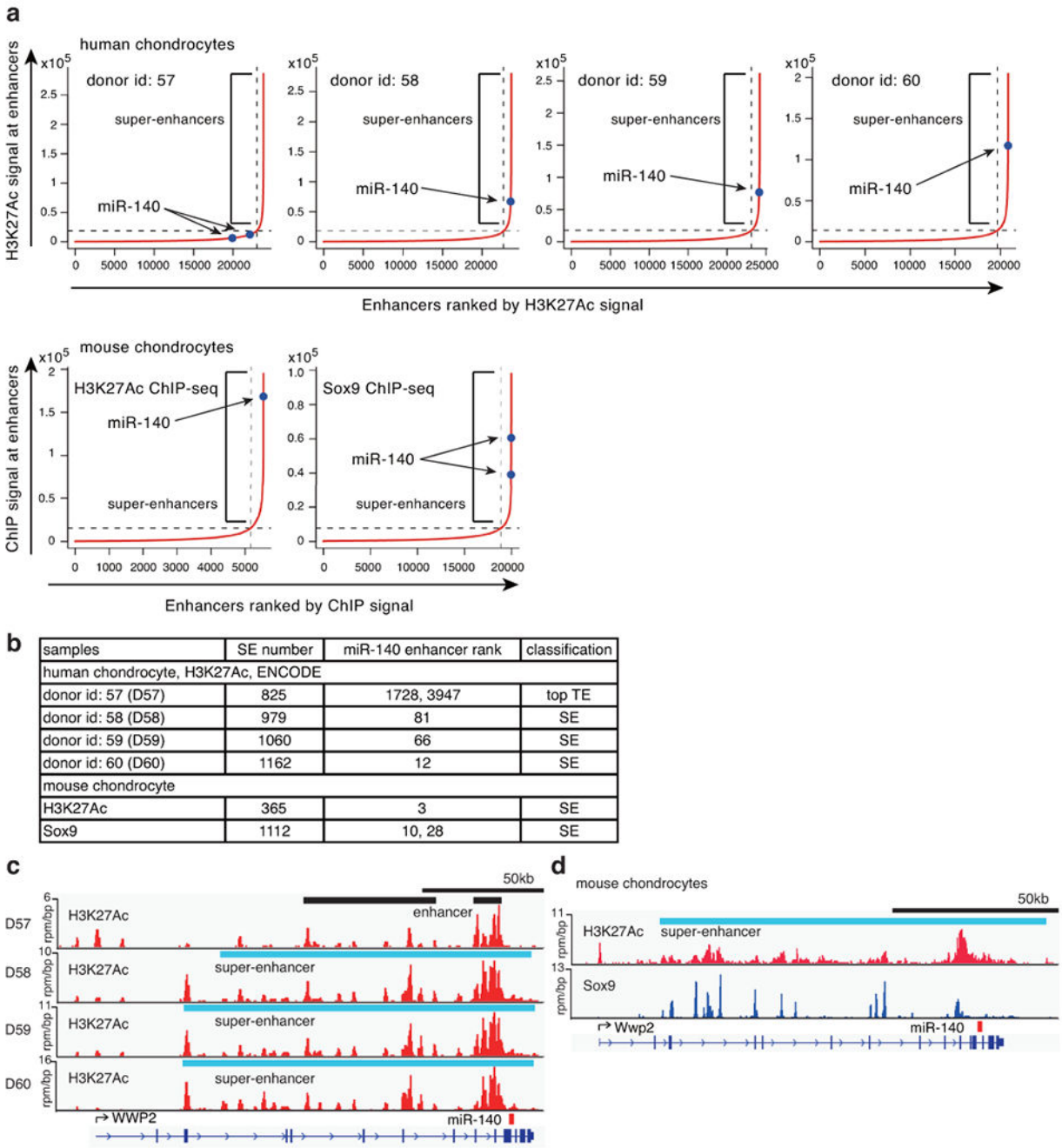

samples	SE number	miR-140 enhancer rank	classification
human chondrocyte, H3K27Ac, ENCODE			
donor id: 57 (D57)	825	1728, 3947	top TE
donor id: 58 (D58)	979	81	SE
donor id: 59 (D59)	1060	66	SE
donor id: 60 (D60)	1162	12	SE
mouse chondrocyte			
H3K27Ac	365	3	SE
Sox9	1112	10, 28	SE

Extended Data Figure. 2. The miR-140 gene-associated super-enhancers in human and mouse chondrocytes.

a, Distribution of ChIP-seq signals at enhancers in human and mouse chondrocytes. The miR-140 gene-associated enhancers are highlighted. The miR-140 locus is associated with high ChIP-seq signals of H3K27Ac and Sox9 in mouse chondrocytes.

b, Summary of association between miR-140 and super-enhancers (SEs). TE: typical enhancer.

c, H3K27Ac ChIP-seq profiles at the miR-140 gene locus in human chondrocytes. The H3K27Ac profile of the donor id: 60 is shown in Fig. 1s.

d, H3K27Ac and Sox9 ChIP-seq profiles of the miR-140 gene locus in mouse chondrocytes.

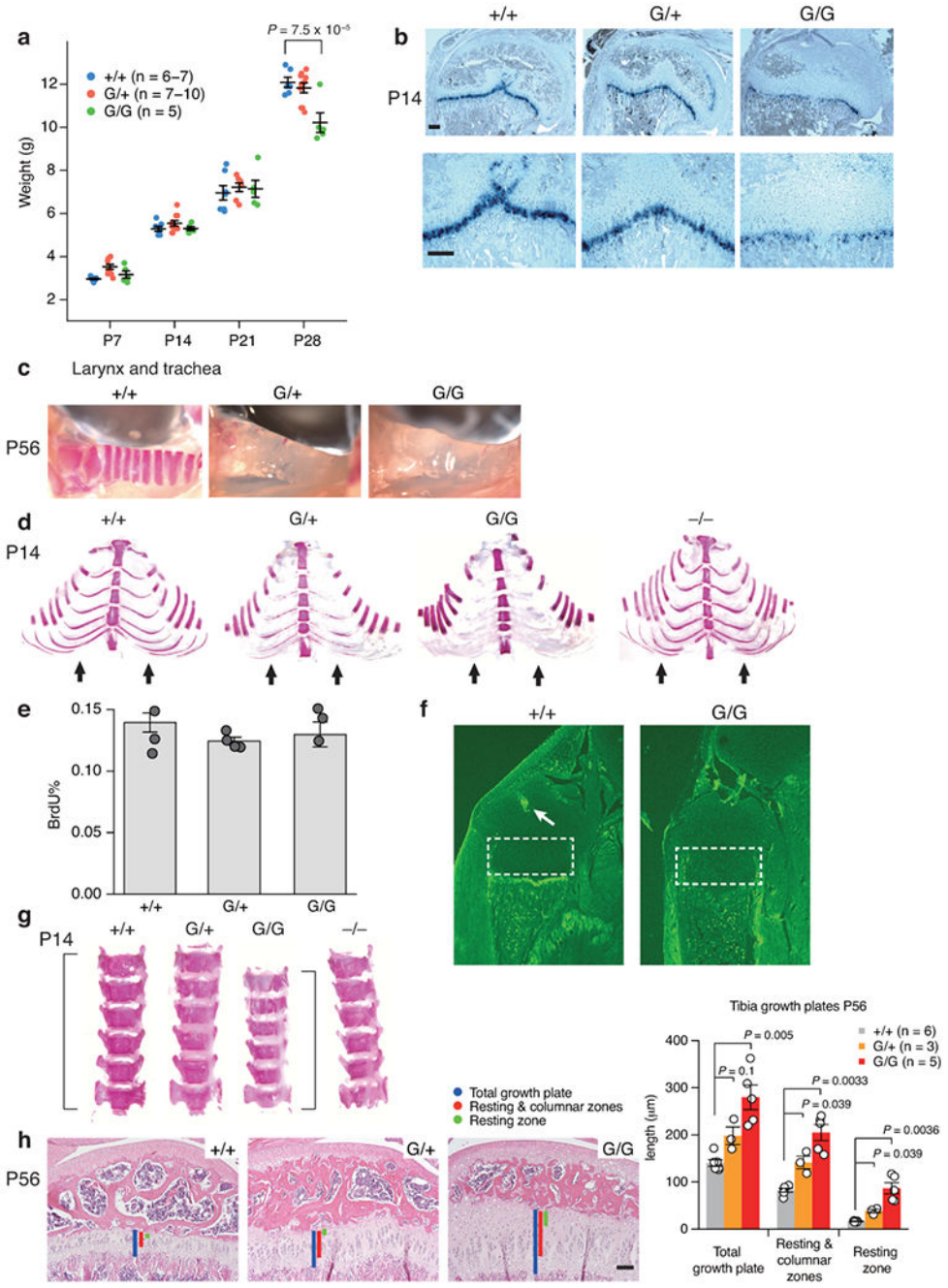

Extended Data Figure. 3. Skeletal phenotype of miR-140 A>G mutant mice.

a, miR-140$^{G/G}$ mice are smaller. The *y* axis and *x* axis indicate weight in grams and days of postnatal age, respectively. Numbers of evaluated mice with indicated genotypes are shown in parentheses. Results represent mean ± s.e.m. Statistical significance was assessed using two-way ANOVA and *post hoc* Tukey-Kramer test.

b, Representative images from two independent experiments (at least three sections of each genotype) of *in situ* hybridization in epiphyseal growth plates of proximal humeri. Decreased expression of *Col10a1* is observed in miR-140$^{G/G}$ and miR-140$^{G/+}$ mice.

c, Representative images of Alizarin red staining of the trachea (+/+, n = 6; G/+, n = 3; G/G, n = 5). Cartilage mineralization is absent or severely impaired in miR-140$^{G/+}$ and miR-140$^{G/G}$ mice.

d, Representative images of Alizarin red staining of the thoracic cage (+/+, n = 4; G/+, n = 7; G/G, n = 9; −/−, n = 2). Delay in chondrocyte mineralization in the rib cartilage is observed in miR-140$^{G/G}$ and miR-140$^{G/+}$ mice.

e, f, Proliferation rate assessed by BrdU labeling (**e**) and apoptosis assessed by TUNEL staining (**f**) in P7 tibial proximal growth plates. The fraction of BrdU positive cells was calculated in the columnar proliferating chondrocytes. Results represent mean ± s.e.m. (+/+, n = 3; G/+, n = 4; G/G, n = 3). Apoptotic cells were not observed in the growth plate of miR-140$^{G/G}$ or miR-140$^{+/+}$ mice (**f**). White arrow indicates apoptotic cells associated with blood vessels invaded into the epiphysis of wild type mice. White dotted boxes indicate the growth plates (excluding the epiphyseal cartilage), and there were no TUNEL-positive cells in the growth plate cartilage in both miR-140$^{+/+}$ and miR-140$^{G/G}$ mice.

g, Representative images of Alizarin red staining of vertebral bodies (+/+, n = 4; G/+, n = 7; G/G, n = 9; −/−, n = 2). Vertebral bodies of miR-140$^{G/G}$ mice are smaller compared with miR-140G/+, miR-140$^{+/+}$, and miR-140$^{-/-}$ mice.

h, Delayed maturation of the proximal tibial epiphysis in P56-old mutant mice. Scale bars, 200μm. Measurements of tibial growth plates of P56 mice show significant expansions in miR-140$^{G/G}$ and miR-140$^{G/+}$ mice. The bar graphs show mean ± s.e.m. (+/+, n = 6; G/+, n = 3; G/G, n = 5). Statistical significance was assessed using Kruskal-Wallis one-way ANOVA and *post hoc* Steel-Dwass test.

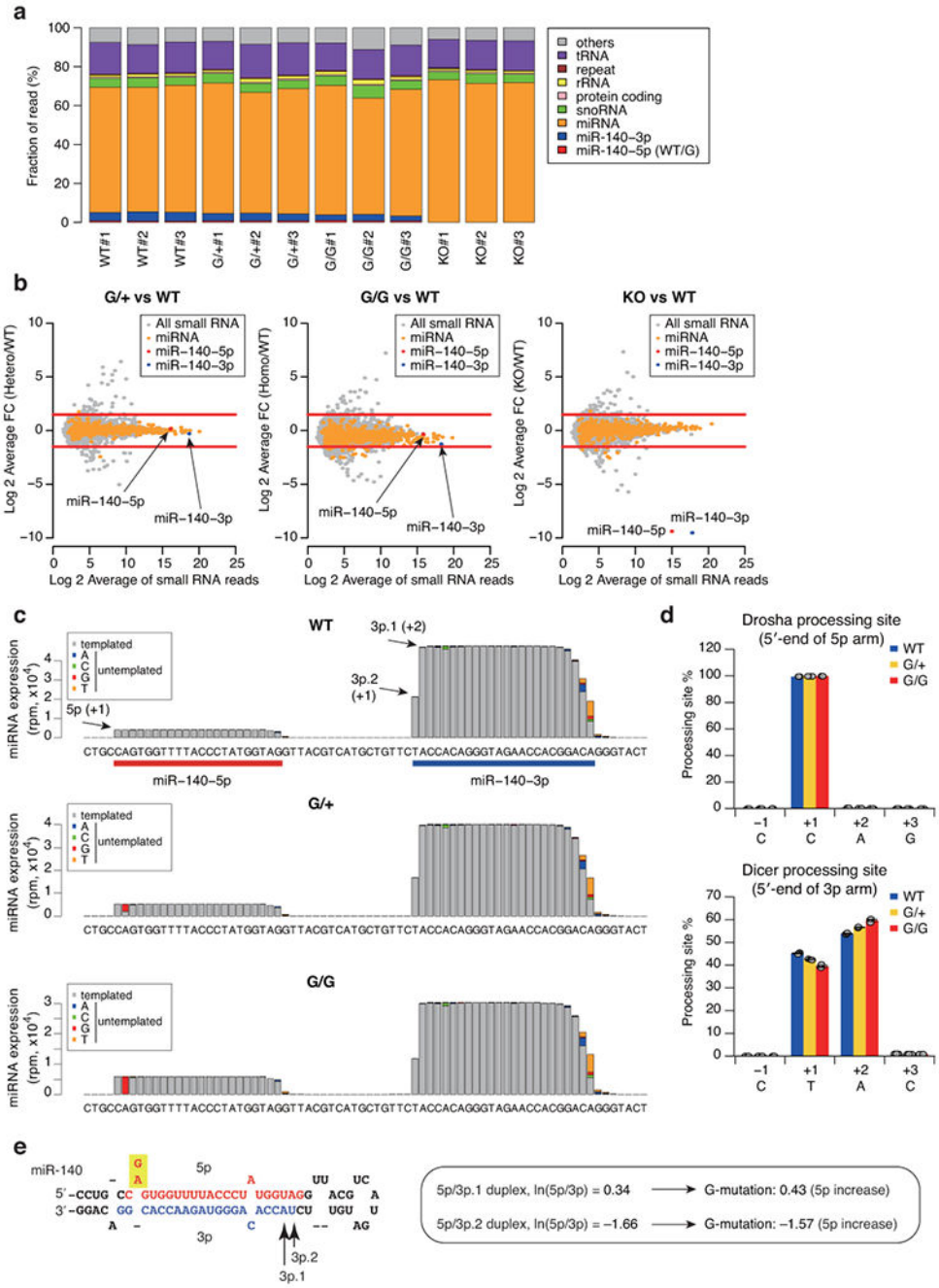

Extended Data Figure. 4. Small RNA profiles in miR-140-G mutant chondrocytes.

a, Proportion of small RNA species of mouse primary chondrocytes with indicated genotypes.

b, Relative fold changes and mean expression levels of small RNAs in WT chondrocytes vs. mutant chondrocytes. Note that miR-140-5p and miR-140-3p are highly abundant miRNAs in chondrocytes, reflecting super-enhancer-mediated high transcriptional activity. Red lines denote 2-fold cutoffs. Significant changes of other miRNAs are not observed.

c, Pileup plots of miR-140-5p and miR-140-3p in WT and mutant chondrocytes.

d, Comparison of Drosha and Dicer processing sites in WT and mutant chondrocytes. Drosha and Dicer cleavage sites were inferred from the 5′-ends of miR-140-5p and miR-140-3p, respectively. Results represent mean ± s.e.m. (n = 3 animals).

e, Predicted effects of the A>G substitution on miR-140 5p/3p ratio. Selection of a single mature miRNA strand from miRNA duplex is determined by combination of 5′-end nucleotide identity and thermodynamic asymmetry of miRNA duplex termini (Ref. 20). Ago2 prefers strands with 5′-uridine or 5′-adenosine and thermodynamically unstable 5′-ends. This mechanistically explains abundant expression of miR-140-3p compared with miR-140-5p in chondrocytes. Prediction of 5p/3p ratio was performed according to our previous report (Ref. 20). Note that the A>G substitution is predicted to destabilize the 5′-end of the 5p arm and thus to increase the 5p/3p ratio for both 5p/3p.1 and 5p/3p.2 duplexes, consistent with the increase in miR-140-5p and decrease in miR-140-3p in chondrocytes from miR-140$^{G/+}$ and miR-140$^{G/G}$ mice.

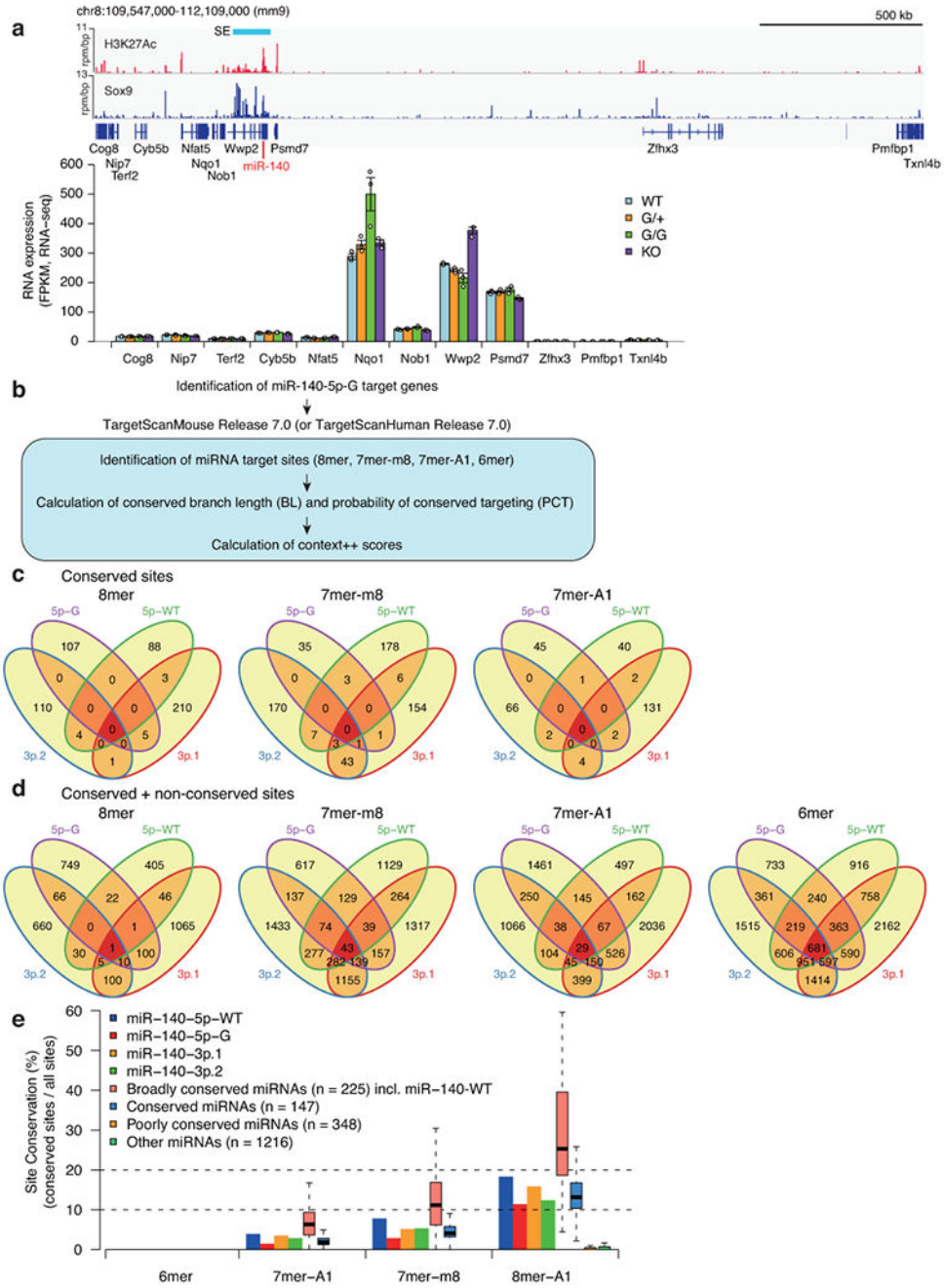

Extended Data Figure. 5. Transcriptome analysis by RNA-seq and identification of miR-140-5p-G targets by TargetScan.

a, Expression levels of genes within the neighborhood of the miR-140 gene locus. Results represent mean ± s.e.m. (n = 3 animals).

b, Workflow of target prediction by TargetScan V7.0.

c, d, Venn Diagrams showing overlaps of genes with conserved sites (**c**) and genes with conserved and non-conserved sites (**d**) for miR-140-5p-WT, -5p-G, -3p.1, and -3p.2.

e, Conservation frequency of target sites for miR-140-5p-WT, -5p-G, -3p.1, and -3p.2. The target sites of miR-140-5p-G are less conserved than those of wild-type miR-140 species. Classification of miRNAs (broadly conserved, conserved, poorly conserved, and others) is based on the TargetScan information. Center lines show medians; box limits indicate the twenty-fifth and seventy-fifth percentiles; whiskers extend to 1.5x the interquartile range.

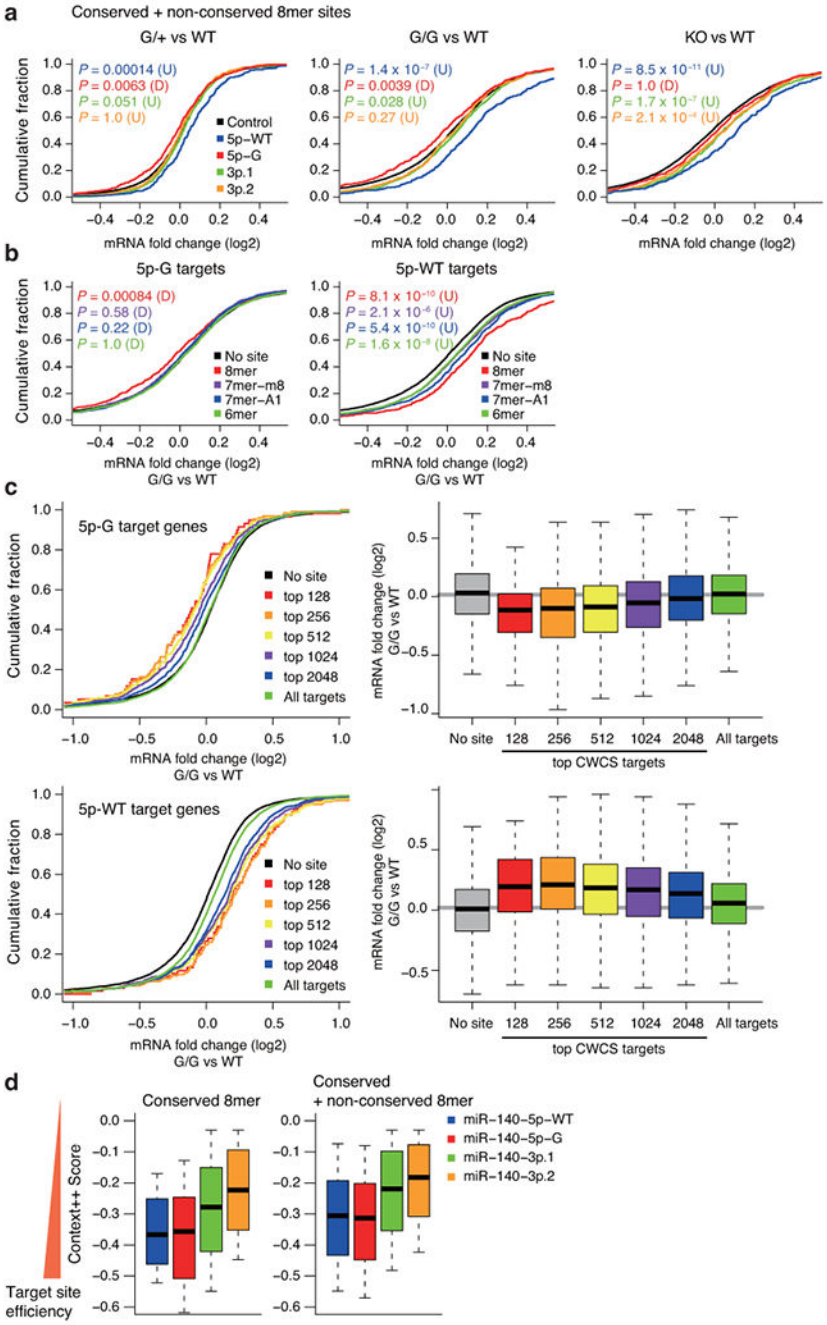

Extended Data Figure. 6. Deregulation of miR-140-5p-G targets in miR-140 mutant chondrocytes.

a, Cumulative distributions of fold changes of mRNAs with conserved and non-conserved 8mer target sites for miR-140-5p-WT, -5p-G, -3p.1, and -3p.2 between miR-140 mutant or null chondrocytes vs. wild-type chondrocytes. P values (versus a control gene set) were calculated by one-sided Kolmogorov–Smirnov (K-S) test for either direction: upregulation (U) or downregulation (D) with Bonferroni correction (Control genes, n = 9706; miR-140-5p-WT, n = 333; miR-140-5p-G, n = 608; miR-140-3p.1, n = 903; miR-140-3p.2, n = 603).

b, Cumulative distributions of fold changes of mRNAs with all 8mer, 7mer-m8, 7mer-A1, and 6mer target sites for miR-140-5p-G (left) and miR-140-5p-WT (right) when comparing miR-140-G homozygous chondrocytes with wild-type chondrocytes. P values (versus a control gene set) were calculated by one-sided Kolmogorov–Smirnov (K-S) test for either direction: upregulation (U) or downregulation (D) with Bonferroni correction. Left (miR-140-5p-G): No site, n = 7684; 8mer, n = 608; 7mer-m8, n = 862; 7mer-A1, n = 1741; 6mer, n = 2497. Right (miR-140-5p-WT): No site, n = 7453; 8mer, n = 333; 7mer-m8, n = 1507; 7mer-A1, n = 710; 6mer, n = 3093.

c, Performance of TargetScan v7 for prediction of miR-140-5p-G targeting. Cumulative distribution plots (left) and box plots (right) of fold change expression of predicted target gene sets grouped by the cumulative weighted context++ score (CWCS). Expression levels of predicted target genes of miR-140-5p-G (top, No site, n = 7684; top 128, n = 59; top 256, n = 129; top 512, n = 275; top 1024, n = 559; top 2048, n = 1178; All targets, n = 4187) and miR-140-5p-WT (bottom, No site, n = 7453; top 128, n = 68; top 256, n = 142; top 512, n = 311; top 1024, n = 637; top 2048, n = 1235; All targets, n = 4418) were analyzed. Gene expression of miR-140-G homozygous chondrocytes and wild-type chondrocytes was compared. All predictions were considered. High CWCS was associated with stronger target gene regulation for both miR-140-5p-G and miR-140-5p-WT, suggesting that miR-140-5p-G follows mechanisms of conventional miRNA targeting as well as other endogenous miRNAs. In box plots, center lines show medians; box limits indicate the twenty-fifth and seventy-fifth percentiles; whiskers extend to 1.5x the interquartile range.

d, Box plots showing context++ scores for conserved (left) and all (right) predicted target sites for miR-140-5p-WT, -5p-G, -3p.1, and -3p.2. Consistent with the effects on target gene expression, miR-140-5p-WT and miR-140-5p-G show similar and higher predicted target site efficiency than miR-140-3p.1 and miR-140-3p.2. Center lines show medians; box limits indicate the twenty-fifth and seventy-fifth percentiles; whiskers extend to 1.5x the interquartile range. Left (Conserved 8mer): miR-140-5p-WT, n = 96; miR-140-5p-G, n = 114; miR-140-3p.1, n = 222; miR-140-3p.2, n = 115. Right (Conserved and non-conserved 8mer): miR-140-5p-WT, n = 524; miR-140-5p-G, n = 1002; miR-140-3p.1, n = 1405; miR-140-3p.2, n = 930.

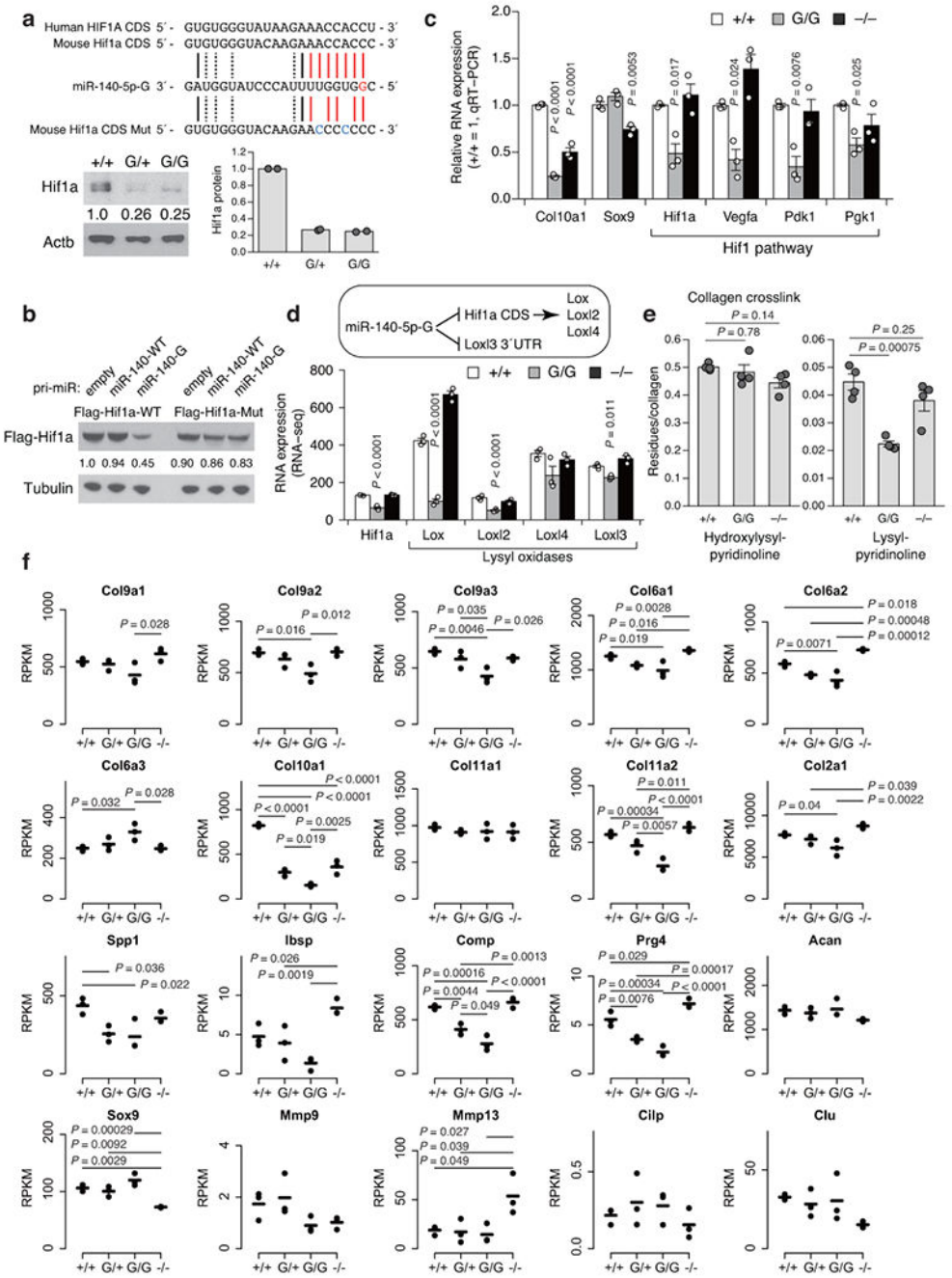

Extended Data Figure. 7. Deregulation of the Hif1a pathway and the cartilage markers in miR-140 mutant chondrocytes.

a, (top) Sequence alignments between miR-140-5p-G and its putative binding sites in the coding sequence of mouse and human *Hif1a*. (bottom) Representative images from two independent experiments of Western blot analysis of Hif1a protein expression in primary rib chondrocytes at the normoxic condition. Hif1a protein was detected by Western blot analysis using anti-Hif1a antibody (Novus Biologicals NB100-449). Bar graphs represent mean (n = 2 animals).

b, Validation of the Hif1a target site. HEK293T cells were transfected with wild-type or mutant mouse Hif1a expression plasmids and pri-miRNA expression plasmids, and subjected to Western blot analysis. Representative images from two independent experiments are shown. A mutation of the target site is shown in panel (a).

c, Relative expression of *Hif1a* and its target genes was determined by qRT-PCR in primary rib chondrocytes isolated from P7 mice. Results represent mean ± s.e.m. (n = 3 animals). Statistical significance was assessed using one-way ANOVA and *post hoc* Tukey-Kramer test. P values indicate comparison versus WT.

d, Expression of lysyl oxidases in P7 primary rib chondrocytes assessed by RNA-seq. Results represent mean ± s.e.m. (n = 3 animals). Statistical significance was assessed using one-way ANOVA and *post hoc* Tukey-Kramer test. P values indicate comparison versus WT.

e, Reduced collagen crosslinking in miR-140$^{G/G}$ rib cartilage cells. Rib cartilage of 4 week-old mice was subjected to collagen crosslink analysis by mass spectrometry. Hydroxylysyl pyridinoline and lysyl pyridinoline were quantified. Results represent mean ± s.e.m. (n = 4 animals). Statistical significance was assessed using one-way ANOVA and *post hoc* Tukey-Kramer test. P values indicate comparison versus WT.

f, RNA expression of cartilage markers. The *x* axis and *y* axis indicate miR-140 genotypes and normalized expression (reads per kilo base per million mapped reads, RPKM), respectively. Each dot represents the expression level in an individual sample (n = 3 animals), and the thick bars indicate the mean value. Statistical significance was assessed using one-way ANOVA and *post hoc* Tukey-Kramer test. Connector lines at the top of each panel indicate significant changes in expression ($P < 0.05$).

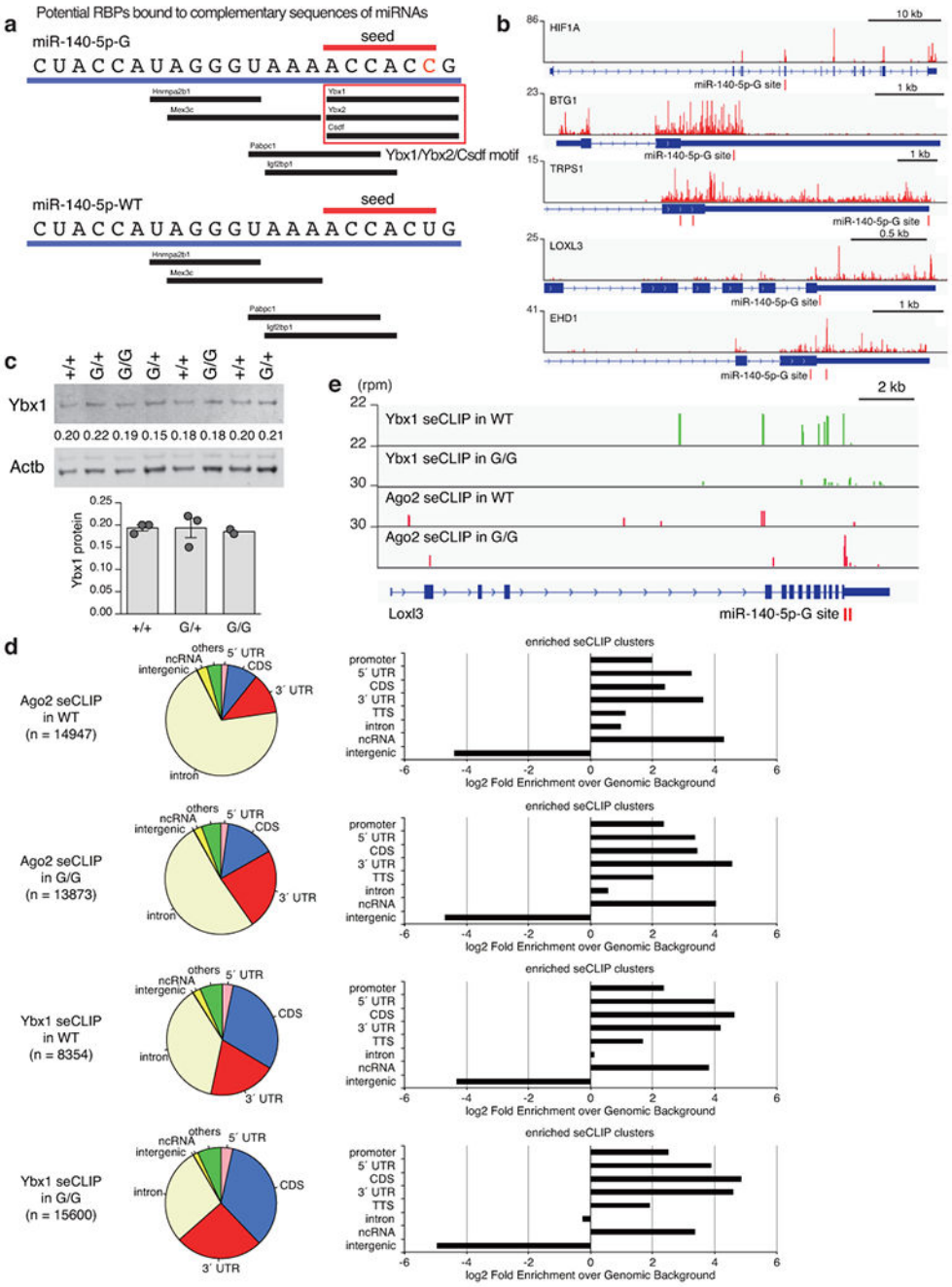

Extended Data Figure. 8. A relationship between miR-140-5p-G and Ybx1 and Ago2 and Ybx1 seCLIP analysis in mouse primary chondrocytes.

a, Potential RNA binding proteins that are predicted to bind to complementary sequences of miR-140-5p-G (left) and miR-140-5p-WT (right). Motif analysis was performed using the CISBP-RNA database.

b, Genome browser shot of YBX1 iCLIP for human *HIF1A, BTG1, TRPS1, LOXL3*, and *EHD1* using the previously reported YBX1 iCLIP data in human glioblastoma cells (Ref.

32). We observed that multiple conserved miR-140-5p-G target genes were bound by YBX1 in the YBX1 iCLIP dataset.

c, Expression levels of Ybx1 protein in mouse primary chondrocytes. Representative images from three independent experiments are shown. Note that Ybx1 protein expression levels normalized to those of Actb did not differ between wild-type and mutant chondrocytes. Normalized values of densitometric analysis are indicated. Results represent mean ± s.e.m. (+/+, n = 3; G/+, n = 3; G/G, n = 2).

d, Genomic annotation of Ago2 and Ybx1 seCLIP clusters. Left pie charts shows genomic distribution of Ago2 and Ybx1 seCLIP clusters. Right panels show the fold enrichment of various genomic annotations over the background.

e, Genome browser shot of the Loxl3 locus.

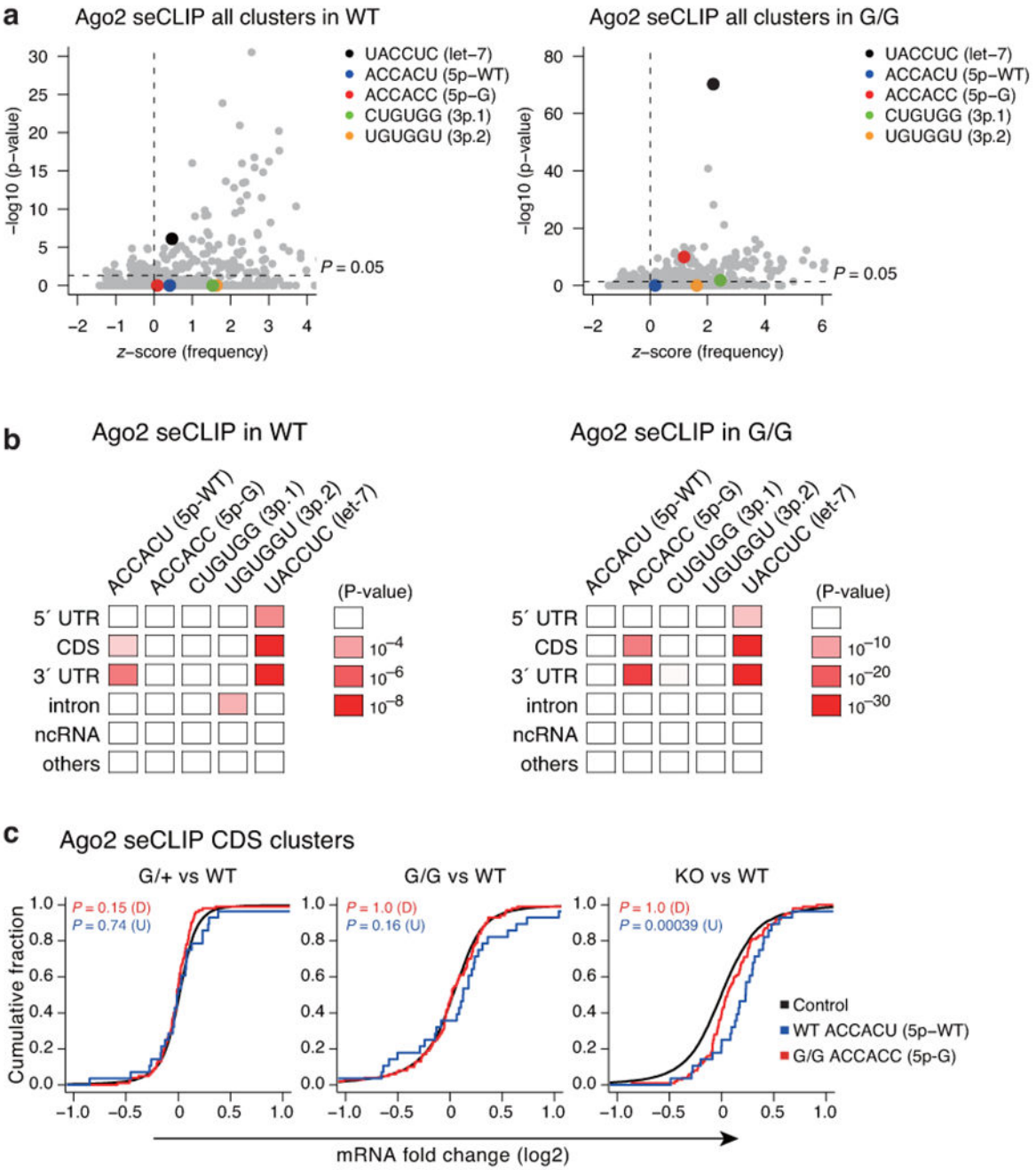

Extended Data Figure. 9. Analysis of Ago2 seCLIP clusters.

a, Hexamer enrichment analysis in all Ago2-bound seCLIP clusters including intronic clusters identified in wild-type (left) and mutant (right) chondrocytes (WT, n = 14947 clusters; G/G, n = 13873 clusters). The *x* axis shows z-scores of hexamer frequency. The *y* axis shows the negative log10 P value from two-sided Fisher's exact test with Bonferroni correction of the hexamer enrichment above background.

b, Hexamer enrichment analysis for various genomic annotations. The negative log10 P values from one-sided Fisher's exact test with Bonferroni correction of the hexamer

enrichment above background are shown. Left (Ago2 WT): 5′ UTR clusters, n = 279; CDS clusters, n = 1315; 3′ UTR clusters, n = 1782; intronic clusters, n = 10402; ncRNA region clusters, n = 434; others, n = 735. Right (Ago2 G/G): 5′ UTR clusters, n = 303; CDS clusters, n = 2006; 3′ UTR clusters, n = 3229; intronic clusters, n = 7091; ncRNA region clusters, n = 332; others, n = 912.

c, Cumulative distributions of fold changes of mRNAs with Ago2-bound seCLIP CDS clusters with the ACCACC motif in mutant chondrocytes (red) or Ago2-bound seCLIP CDS clusters with the ACCACU motif in wild-type chondrocytes. P values (versus a control gene set) were calculated by one-sided Kolmogorov–Smirnov (K-S) test for either direction: upregulation (U) or downregulation (D) with Bonferroni correction (Control genes, n = 10093; miR-140-5p-WT, n = 28; miR-140-5p-G, n = 100).

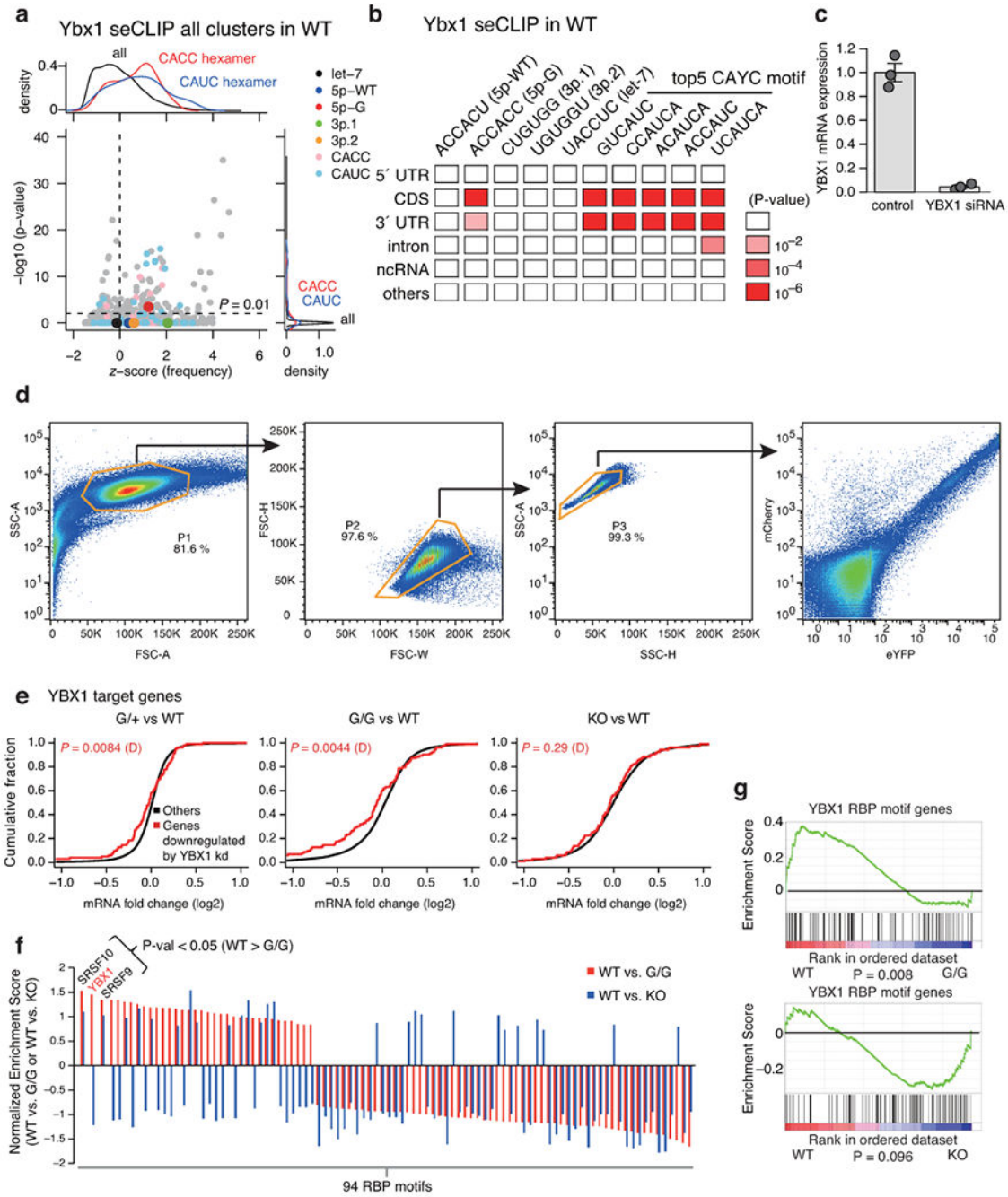

Extended Data Figure. 10. Analysis of Ybx1 seCLIP clusters.

a, Hexamer enrichment analysis in all Ybx1-bound seCLIP clusters including intronic clusters, identified in wild-type chondrocytes (n = 8354). The *x* axis shows the *z*-scores of hexamer frequency. The y axis shows the negative log10 P value of two-sided Fisher's exact test with Bonferroni correction of the hexamer enrichment above background.

b, Hexamer enrichment analysis for various genomic annotations (5′ UTR clusters, n = 265; CDS clusters, n = 2537; 3′ UTR clusters, n = 1649; intronic clusters, n = 3143; ncRNA region clusters, n = 191; others, n = 569). The negative log10 P values from one-sided

Fisher's exact test with Bonferroni correction of the hexamer enrichment above background are shown.

c, siRNA-mediated knockdown of YBX1 in HEK293T cells for single-cell reporter analysis, confirmed by qRT-PCR analysis. Results represent mean ± s.e.m. (n = 3 biologically independent samples).

d, Flow cytometry gating strategies for single-cell reporter analysis. Single-cell populations (P3) were selected by sequential gating by SSC and FSC and subjected to two-color analysis in Fig. 4i. An example of the flow cytometry gating strategy is shown.

e, Cumulative distributions of fold changes of YBX1-stablized gene sets between miR-140 mutant or null chondrocytes vs. wild-type chondrocytes. P values (versus a control gene set) were calculated by one-sided Kolmogorov–Smirnov (K-S) test for downregulation (D) (Other genes, n = 11768; YBX1-regulated genes, n = 103).

f, g, Systematic RBP target gene analysis using GSEA. For 94 RBPs, possible RBP target genes were predicted using RBPmap (Ref. 59), and used for GSEA analysis to assess which RBP activity changes in miR-140-G homozygous and miR-140-null chondrocytes relative to WT chondrocytes (n = 3 animals for each group). In panel (**f**), normalized enrichment scores for 94 RBPs are shown. Among three significantly suppressed motifs in miR-140-G homozygous cells (SRSF10, YBX1, and SRSF9), only the YBX1 RBP motif gene set was selectively suppressed in miR-140-G homozygous but not miR-140-null cells. In panel (**g**), GSEA enrichment plots for YBX1 RBP motif genes are shown. Enrichment analysis and statistical analysis were performed using GSEA.

Supplementary Material

Refer to Web version on PubMed Central for supplementary material.

Acknowledgements

We thank patients and their family members for their participation in the study, M. Mannstadt, K. Leuter, M. Wein, H. Kronenberg, H. Jueppner, G. Björk, and A. Merker for advice and chemicals, J. Lundin for assistance with the human CGH array databases, and Science for Life Laboratory, the National Genomics Infrastructure (NGI), Sweden, SNIC through UPPMAX under project b2014231 for providing assistance in massive parallel DNA sequencing and computational infrastructure.

We also thank Center for Skeletal Research Core (NIH P30 AR066261) for access to histological analysis equipment; Harvard GMF for generation of knock-in mice; and DFCI and MGH Sequencing Cores for assistance with RNA and Sanger sequencing; the Robert A. Swanson (1969) Biotechnology Center at the Koch Institute for Integrative Cancer Research at Massachusetts Institute of Technology for technical support, specifically S. Levine and the staff of the BioMicro Center/KI Genomic Core Facility and G. Paradis, M. Jennings, and M. Saturno-Condon of the Flow Cytometry Core Facility.

This project was supported by grants provided by the Stockholm County Council (ALF projects 20150143 and 20130315 to G. Grigelioniene. and A.N.) and by the National Institutes of Health (National Institute of Arthritis and Musculoskeletal and Skin Diseases grant R01-AR056645 to T.K., National Institute of General Medical Sciences grant R01-GM034277 and National Cancer Institute grant R01-CA133404 to P.A.S., and National Cancer Institute grant P30-CA14051 to the Koch Institute Core Facility).

G. Grigelioniene was supported by a grant of the Sabbatical Leave Programme of the European Society for Paediatric Endocrinology through an educational grant from Eli Lilly International Corporation, travel grants from Fernström Foundation, Karolinska Institutet and Swedish Society of Medicine, scholarship from Stiftelsen Samariten, Stockholm, Sweden, Research Funds from Promobilia and Frimurare Barnhuset Stockholm, and project grant from Swedish Research Council 2018-03046. H.I.S. is supported by the Uehara Memorial Foundation Research Fellowship and the Osamu Hayaishi Memorial Scholarship for Study Abroad.

References

1. Mencia A, et al. Mutations in the seed region of human miR-96 are responsible for nonsyndromic progressive hearing loss. Nat Genet 41, 609–613 (2009). [PubMed: 19363479]
2. Solda G, et al. A novel mutation within the MIR96 gene causes non-syndromic inherited hearing loss in an Italian family by altering pre-miRNA processing. Hum Mol Genet 21, 577–585 (2012). [PubMed: 22038834]
3. Hughes AE, et al. Mutation altering the miR-184 seed region causes familial keratoconus with cataract. Am J Hum Genet 89, 628–633 (2011). [PubMed: 21996275]
4. Iliff BW, Riazuddin SA & Gottsch JD A single-base substitution in the seed region of miR-184 causes EDICT syndrome. Invest Ophthalmol Vis Sci 53, 348–353 (2012). [PubMed: 22131394]
5. Lechner J, et al. Mutational analysis of MIR184 in sporadic keratoconus and myopia. Invest Ophthalmol Vis Sci 54, 5266–5272 (2013). [PubMed: 23833072]
6. Nakamura Y, Inloes JB, Katagiri T & Kobayashi T Chondrocyte-specific microRNA-140 regulates endochondral bone development and targets Dnpep to modulate bone morphogenetic protein signaling. Mol Cell Biol 31, 3019–3028 (2011). [PubMed: 21576357]
7. Chen K & Rajewsky N The evolution of gene regulation by transcription factors and microRNAs. Nat Rev Genet 8, 93–103 (2007). [PubMed: 17230196]
8. Berezikov E Evolution of microRNA diversity and regulation in animals. Nat Rev Genet 12, 846–860 (2011). [PubMed: 22094948]
9. Bonafe L, et al. Nosology and classification of genetic skeletal disorders: 2015 revision. Am J Med Genet A 167A, 2869–2892 (2015). [PubMed: 26394607]
10. Lek M, et al. Analysis of protein-coding genetic variation in 60,706 humans. Nature 536, 285–291 (2016). [PubMed: 27535533]
11. Suzuki HI, Young RA & Sharp PA Super-Enhancer-Mediated RNA Processing Revealed by Integrative MicroRNA Network Analysis. Cell 168, 1000–1014 e1015 (2017). [PubMed: 28283057]
12. Whyte WA, et al. Master transcription factors and mediator establish super-enhancers at key cell identity genes. Cell 153, 307–319 (2013). [PubMed: 23582322]
13. Hnisz D, et al. Super-enhancers in the control of cell identity and disease. Cell 155, 934–947 (2013). [PubMed: 24119843]
14. Wienholds E, et al. MicroRNA expression in zebrafish embryonic development. Science 309, 310–311 (2005). [PubMed: 15919954]
15. Tuddenham L, et al. The cartilage specific microRNA-140 targets histone deacetylase 4 in mouse cells. FEBS Lett 580, 4214–4217 (2006). [PubMed: 16828749]
16. Miyaki S, et al. MicroRNA-140 plays dual roles in both cartilage development and homeostasis. Genes Dev 24, 1173–1185 (2010). [PubMed: 20466812]
17. Papaioannou G, et al. MicroRNA-140 Provides Robustness to the Regulation of Hypertrophic Chondrocyte Differentiation by the PTHrP-HDAC4 Pathway. J Bone Miner Res 30, 1044–1052 (2015). [PubMed: 25529628]
18. Ran FA, et al. Genome engineering using the CRISPR-Cas9 system. Nat Protoc 8, 2281–2308 (2013). [PubMed: 24157548]
19. Park JE, et al. Dicer recognizes the 5’ end of RNA for efficient and accurate processing. Nature 475, 201–205 (2011). [PubMed: 21753850]
20. Suzuki HI, et al. Small-RNA asymmetry is directly driven by mammalian Argonautes. Nat Struct Mol Biol 22, 512–521 (2015). [PubMed: 26098316]
21. Agarwal V, Bell GW, Nam JW & Bartel DP Predicting effective microRNA target sites in mammalian mRNAs. Elife 4(2015).
22. Zhang J, et al. Loss of lysyl oxidase-like 3 causes cleft palate and spinal deformity in mice. Hum Mol Genet 24, 6174–6185 (2015). [PubMed: 26307084]
23. Tijchon E, et al. Targeted Deletion of Btg1 and Btg2 Results in Homeotic Transformation of the Axial Skeleton. PLoS One 10, e0131481 (2015). [PubMed: 26218146]

24. Napierala D, et al. Uncoupling of chondrocyte differentiation and perichondrial mineralization underlies the skeletal dysplasia in tricho-rhino-phalangeal syndrome. Hum Mol Genet 17, 2244–2254 (2008). [PubMed: 18424451]
25. Subramanian A, et al. Gene set enrichment analysis: a knowledge-based approach for interpreting genome-wide expression profiles. Proc Natl Acad Sci U S A 102, 15545–15550 (2005). [PubMed: 16199517]
26. Merico D, Isserlin R, Stueker O, Emili A & Bader GD Enrichment map: a network-based method for gene-set enrichment visualization and interpretation. PLoS One 5, e13984 (2010). [PubMed: 21085593]
27. Wan C, et al. Role of HIF-1alpha in skeletal development. Ann N Y Acad Sci 1192, 322–326 (2010). [PubMed: 20392254]
28. Grimson A, et al. MicroRNA targeting specificity in mammals: determinants beyond seed pairing. Mol Cell 27, 91–105 (2007). [PubMed: 17612493]
29. van Kouwenhove M, Kedde M & Agami R MicroRNA regulation by RNA-binding proteins and its implications for cancer. Nat Rev Cancer 11, 644–656 (2011). [PubMed: 21822212]
30. Ray D, et al. A compendium of RNA-binding motifs for decoding gene regulation. Nature 499, 172–177 (2013). [PubMed: 23846655]
31. Wei WJ, et al. YB-1 binds to CAUC motifs and stimulates exon inclusion by enhancing the recruitment of U2AF to weak polypyrimidine tracts. Nucleic Acids Res 40, 8622–8636 (2012). [PubMed: 22730292]
32. Wu SL, et al. Genome-wide analysis of YB-1-RNA interactions reveals a novel role of YB-1 in miRNA processing in glioblastoma multiforme. Nucleic Acids Res 43, 8516–8528 (2015). [PubMed: 26240386]
33. Lyabin DN, Eliseeva IA & Ovchinnikov LP YB-1 protein: functions and regulation. Wiley Interdiscip Rev RNA 5, 95–110 (2014). [PubMed: 24217978]
34. Goodarzi H, et al. Endogenous tRNA-Derived Fragments Suppress Breast Cancer Progression via YBX1 Displacement. Cell 161, 790–802 (2015). [PubMed: 25957686]
35. Van Nostrand EL, et al. Robust transcriptome-wide discovery of RNA-binding protein binding sites with enhanced CLIP (eCLIP). Nat Methods 13, 508–514 (2016). [PubMed: 27018577]
36. Van Nostrand EL, et al. Erratum to: Robust, Cost-Effective Profiling of RNA Binding Protein Targets with Single-end Enhanced Crosslinking and Immunoprecipitation (seCLIP). Methods Mol Biol 1648, E1 (2017). [PubMed: 29230720]
37. de Pontual L, et al. Germline deletion of the miR-17 approximately 92 cluster causes skeletal and growth defects in humans. Nat Genet 43, 1026–1030 (2011). [PubMed: 21892160]
38. Henrion-Caude A, Girard M & Amiel J MicroRNAs in genetic disease: rethinking the dosage. Curr Gene Ther 12, 292–300 (2012). [PubMed: 22856604]
39. Lewis MA, et al. An ENU-induced mutation of miR-96 associated with progressive hearing loss in mice. Nat Genet 41, 614–618 (2009). [PubMed: 19363478]
40. Suzuki HI, Spengler RM, Grigelioniene G, Kobayashi T & Sharp PA Deconvolution of seed and RNA-binding protein crosstalk in RNAi-based functional genomics. Nat Genet 50, 657–661 (2018). [PubMed: 29662165]

Methods-only References

41. Kaminsky EB, et al. An evidence-based approach to establish the functional and clinical significance of copy number variants in intellectual and developmental disabilities. Genet Med 13, 777–784 (2011). [PubMed: 21844811]
42. Niklasson A & Albertsson-Wikland K Continuous growth reference from 24th week of gestation to 24 months by gender. BMC Pediatr 8, 8 (2008). [PubMed: 18307822]
43. Kvarnung M, et al. Genomic screening in rare disorders: New mutations and phenotypes, highlighting ALG14 as a novel cause of severe intellectual disability. Clin Genet 94, 528–537 (2018). [PubMed: 30221345]
44. Li H & Durbin R Fast and accurate short read alignment with Burrows-Wheeler transform. Bioinformatics 25, 1754–1760 (2009). [PubMed: 19451168]

45. McKenna A, et al. The Genome Analysis Toolkit: a MapReduce framework for analyzing next-generation DNA sequencing data. Genome Res 20, 1297–1303 (2010). [PubMed: 20644199]
46. Okonechnikov K, Conesa A & Garcia-Alcalde F Qualimap 2: advanced multi-sample quality control for high-throughput sequencing data. Bioinformatics 32, 292–294 (2016). [PubMed: 26428292]
47. Lindstrand A, et al. Improved structural characterization of chromosomal breakpoints using high resolution custom array-CGH. Clin Genet 77, 552–562 (2010). [PubMed: 20236111]
48. Yang H, Wang H & Jaenisch R Generating genetically modified mice using CRISPR/Cas-mediated genome engineering. Nat Protoc 9, 1956–1968 (2014). [PubMed: 25058643]
49. Wein MN, et al. SIKs control osteocyte responses to parathyroid hormone. Nat Commun 7, 13176 (2016). [PubMed: 27759007]
50. Eyre D Collagen cross-linking amino acids. Methods Enzymol 144, 115–139 (1987). [PubMed: 3626870]
51. Ohba S, He X, Hojo H & McMahon AP Distinct Transcriptional Programs Underlie Sox9 Regulation of the Mammalian Chondrocyte. Cell Rep 12, 229–243 (2015). [PubMed: 26146088]
52. Langmead B, Trapnell C, Pop M & Salzberg SL Ultrafast and memory-efficient alignment of short DNA sequences to the human genome. Genome Biol 10, R25 (2009). [PubMed: 19261174]
53. Zhang Y, et al. Model-based analysis of ChIP-Seq (MACS). Genome Biol 9, R137 (2008). [PubMed: 18798982]
54. Dobin A, et al. STAR: ultrafast universal RNA-seq aligner. Bioinformatics 29, 15–21 (2013). [PubMed: 23104886]
55. Trapnell C, et al. Transcript assembly and quantification by RNA-Seq reveals unannotated transcripts and isoform switching during cell differentiation. Nat Biotechnol 28, 511–515 (2010). [PubMed: 20436464]
56. Grant GR, et al. Comparative analysis of RNA-Seq alignment algorithms and the RNA-Seq unified mapper (RUM). Bioinformatics 27, 2518–2528 (2011). [PubMed: 21775302]
57. Robinson MD, McCarthy DJ & Smyth GK edgeR: a Bioconductor package for differential expression analysis of digital gene expression data. Bioinformatics 26, 139–140 (2010). [PubMed: 19910308]
58. Zamudio JR, Kelly TJ & Sharp PA Argonaute-bound small RNAs from promoter-proximal RNA polymerase II. Cell 156, 920–934 (2014). [PubMed: 24581493]
59. Paz I, Kosti I, Ares M Jr., Cline M & Mandel-Gutfreund Y RBPmap: a web server for mapping binding sites of RNA-binding proteins. Nucleic Acids Res 42, W361–367 (2014). [PubMed: 24829458]
60. Heinz S, et al. Simple combinations of lineage-determining transcription factors prime cis-regulatory elements required for macrophage and B cell identities. Mol Cell 38, 576–589 (2010). [PubMed: 20513432]

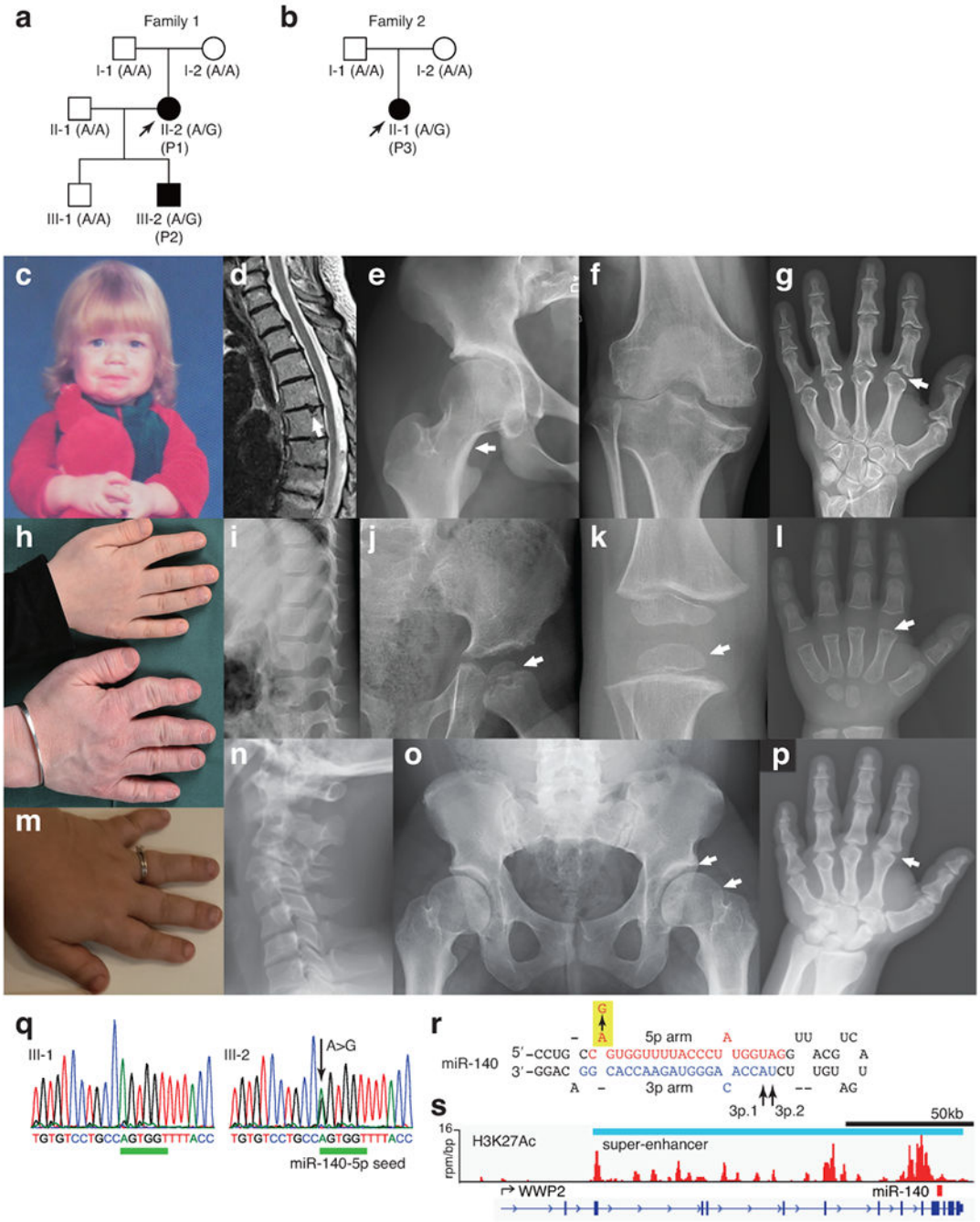

Figure 1. Novel skeletal dysplasia associated with miR-140-5p mutation.

a, b, Pedigrees of Family 1 (**a**) and Family 2 (**b**). Black filled symbols indicate affected individuals; black arrows indicate probands. II-2 and III-2 in Family 1 are P1 and 2, respectively. II-1 in Family 2 denotes P3. The genotype of *MIR140* at the position of the mutation (A/A or A/G) is indicated for each individual in the study.

c, Patient 1 at 2 years of age; note midface hypoplasia and short nose. The patient has kindly provided her childhood photo for publication and the authors have obtained signed proof of informed consent.

d-g, Radiograms of P1 at 40 years of age. Premature degeneration of intervertebral disks in the cervical spine (**d**); hypoplasia of the lower ilium, and short, constricted femoral neck (white arrow) (**e**); premature degenerative changes of the knee joint (**f**); brachydactyly with coning of the proximal phalangeal end, particularly of the second digit (white arrow) (**g**).

h, Brachydactyly and broad thumbs in P1 and her son, P2.

i-l, Radiograms of P2 at 4 years of age. Mild irregularity of vertebral endplates at the thoracolumbar junction (**i**); hypoplasia of the lower ilium, and delayed ossification of the proximal femoral epiphysis (white arrow) (**j**); small epiphyses of the distal femur and proximal tibia (white arrow) (**k**); brachydactyly with delayed epiphyseal maturation (white arrow) (**l**).

m-p, P3 at 30 years of age: note brachydactyly and deformities of interphalangeal joints (**m**); premature disk degeneration in the upper cervical spine (**n**); hypoplasia of the lower ilium, and short femoral necks (white arrows) (**o**); brachydactyly with mild coning of the proximal phalangeal end of the index finger (white arrow) (**p**).

q, Schematic representation of the mutation in miR-140-5p (nucleotides in the seed sequence are marked with green). The mutated nucleotide is indicated by a black arrow.

r, Sequence of miR-140 precursor. Heterogeneity in Dicer processing yields two species of miR-140-3p (3p.1 and 3p.2).

s, H3K27Ac ChIP-seq showing super-enhancers associated with *MIR140* in human chondrocytes.

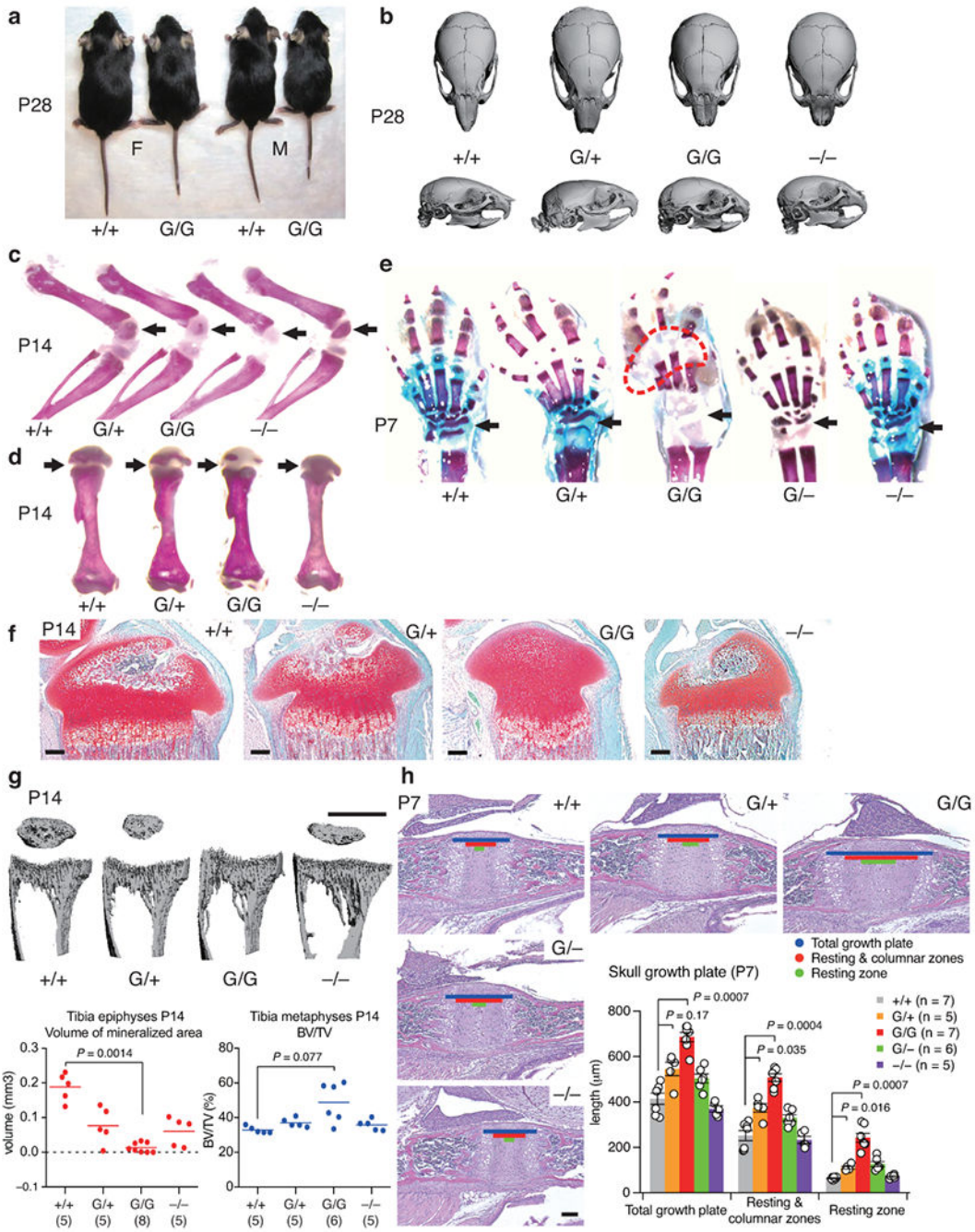

Figure 2. Skeletal phenotype of miR-140 mutant mice

a, Both female (F) and male (M) homozygous miR-140$^{G/G}$ (G/G) mice are smaller in size than wild-type (+/+) littermates at postnatal day 28 (P28) (+/+, n = 6; G/+, n = 10; G/G, n = 5).

b, Micro computer tomography (µCT) scans of the skull at postnatal day 28 (P28), note the shortening of the nasal bone in homozygous (G/G) and miR-140 knockout (−/−) mice.

c-**e**, Skeletal preparation. Delayed secondary ossification (black arrows) in the epiphyses of femura (**c**) and humeri (**d**) of homozygous (G/G) and heterozygous (G/+) mice (+/+, n = 4;

G/+, n = 7; G/G, n = 9; −/−, n = 2). Note that epiphyseal ossification is normal in (−/−) mice. Delayed ossification is similarly present in carpal bones (black arrows) and epiphyses of metacarpals (area marked with a red dashed line) of (G/G), (G/+), and (G/−) mice (**e**) (+/+, n = 7; G/+, n = 6; G/G, n = 8; −/−, n = 5).

f, Representative images from three independent experiments of Safranin O-stained sections of the proximal tibia. Each experiment included duplicate sections of tibia from at least two animals of each genotype Note absence and delay in vascular invasion in (G/G) and (G/+) epiphyses, respectively.

g, μCT analysis showing decreased epiphyseal mineralization in (G/G) mice (+/+, n = 5; G/+, n = 5; G/G, n = 8; −/−, n = 5). All animals used for μCT analysis were males. Note that bone volume and total volume ratios (BV/TV) in the metaphyses do not differ among the different genotypes. Horizontal bars indicate mean values.

h, Hematoxylin and eosin-stained sagittal sections of the cranial base growth plate between the basisphenoid and basioccipital bones. Note significant expansion of the all zones (blue bars, total growth plate; red bars, the proliferating zone containing the resting and columnar zones; green bars the resting zone) in (G/G) compared to (+/+) mice. (G/+) and (G/−) mice also show expansion of the growth plate although to a smaller extent than (G/G) mice. The bar graph shows mean ± s.e.m. (+/+, n = 7; G/+, n = 5; G/G, n = 7; G/−, n = 6; −/−, n = 5). Postnatal ages (P) are indicated in days. Scale bars are 200μm in microscope images and 1 mm in μCT. In panels (**g**) and (**h**), statistical significance was assessed using Kruskal-Wallis one-way analysis of variance (ANOVA) and *post hoc* Steel-Dwass test.

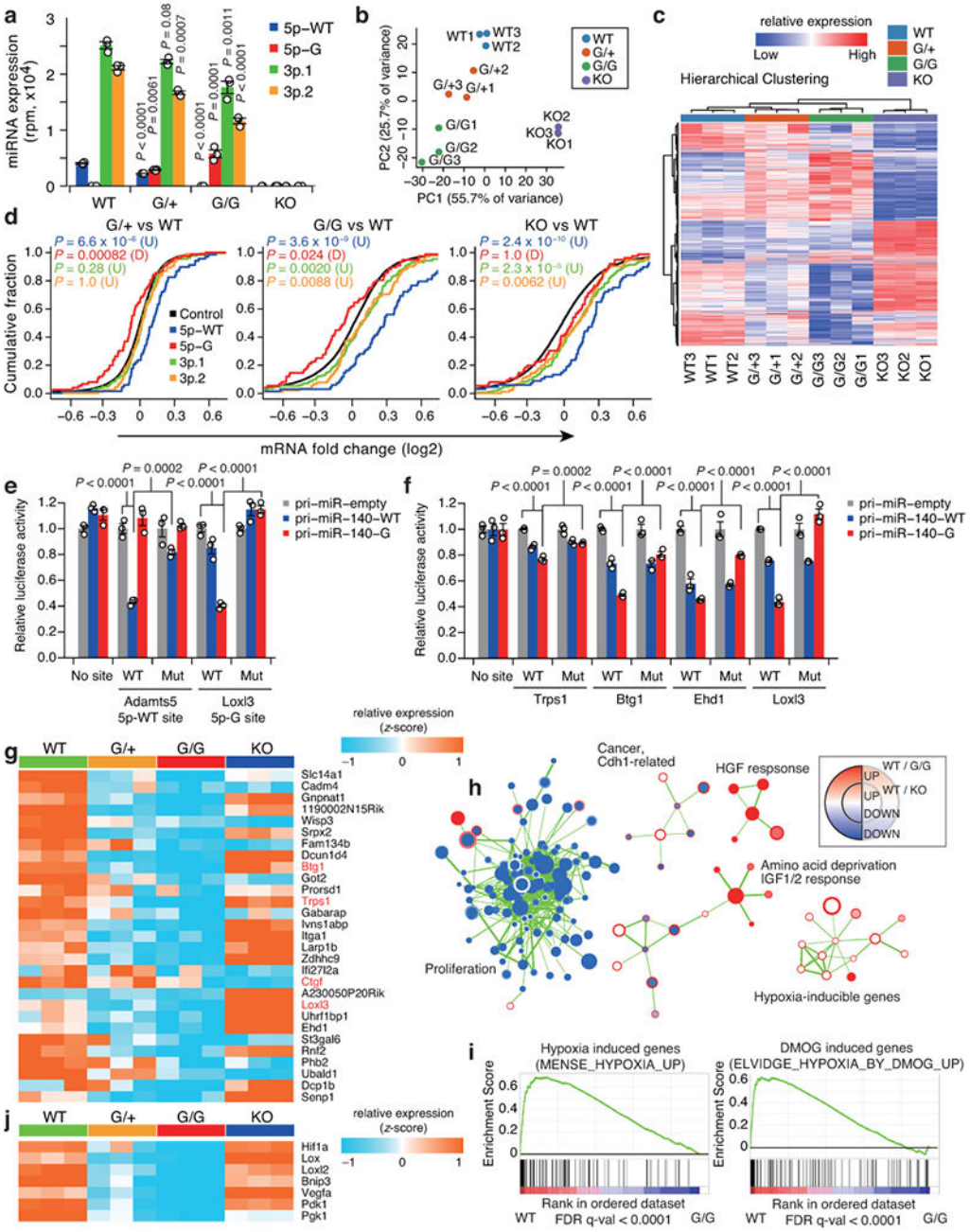

Figure 3. Loss-of-function and gain-of-function effects of miR-140 G mutation in chondrocyte transcriptome

a, Expression levels of miR-140-5p (WT and G mutant) and two species of miR-140-3p (3p. 1 and 3p.2) in primary rib chondrocytes. Rpm: reads per million. Results represent mean ± s.e.m. (n = 3 animals). Statistical significance was assessed using one-way ANOVA and *post hoc* Tukey-Kramer test. P values indicate comparison versus WT.

b, c, Principle component analysis (**b**) and hierarchical clustering (**c**) based on 1000 most variable genes in RNA-seq datasets (n = 3 animals for each group).

d, Cumulative distributions of fold changes of mRNAs with conserved 8mer binding sites for miR-140-5p-WT, -5p-G, -3p.1, and -3p.2 in miR-140 mutant and null chondrocytes. P values (versus a control gene set) were calculated by one-sided Kolmogorov–Smirnov (K-S) test for either direction: upregulation (U) or downregulation (D) with Bonferroni correction (Control genes, n = 11472; miR-140-5p-WT, n = 68; miR-140-5p-G, n = 76; miR-140-3p.1, n = 173; miR-140-3p.2, n = 91).

e, f, Target verification of miR-140-5p-G target sites by 3′ UTR reporter assay in the context of minimal target sites (**e**) and the endogenous 3′ UTR context (**f**). Results represent mean ± s.e.m. (n = 3 biologically independent samples). Statistical significance was assessed using two-way ANOVA and *post hoc* Tukey-Kramer test.

g, Heatmap showing expression changes of representative genes with conserved miR-140-5p-G target sites and downregulation in miR-140$^{G/G}$ chondrocytes. Red denotes important regulators of skeletal development.

h-j, Enrichment map analysis on GSEA results (FDR q-value < 0.1) showing affected cellular programs in miR-140$^{G/G}$ or miR-140-null chondrocytes (**h**), representative GSEA results for hypoxia-induced gene sets (**i**, DMOG: hypoxia mimic), and expression heatmap for major Hif1 target genes (**j**). In (**h**), enrichments in WT vs. miR-140$^{G/G}$ and WT vs. miR-140-null cells are mapped to the node borders and inner node area, respectively. Red and blue represent upregulation and downregulation in WT cells relative to miR-140$^{G/G}$ or miR-140-null cells, respectively. Pathway enrichment analysis and statistical analysis were performed using GSEA.

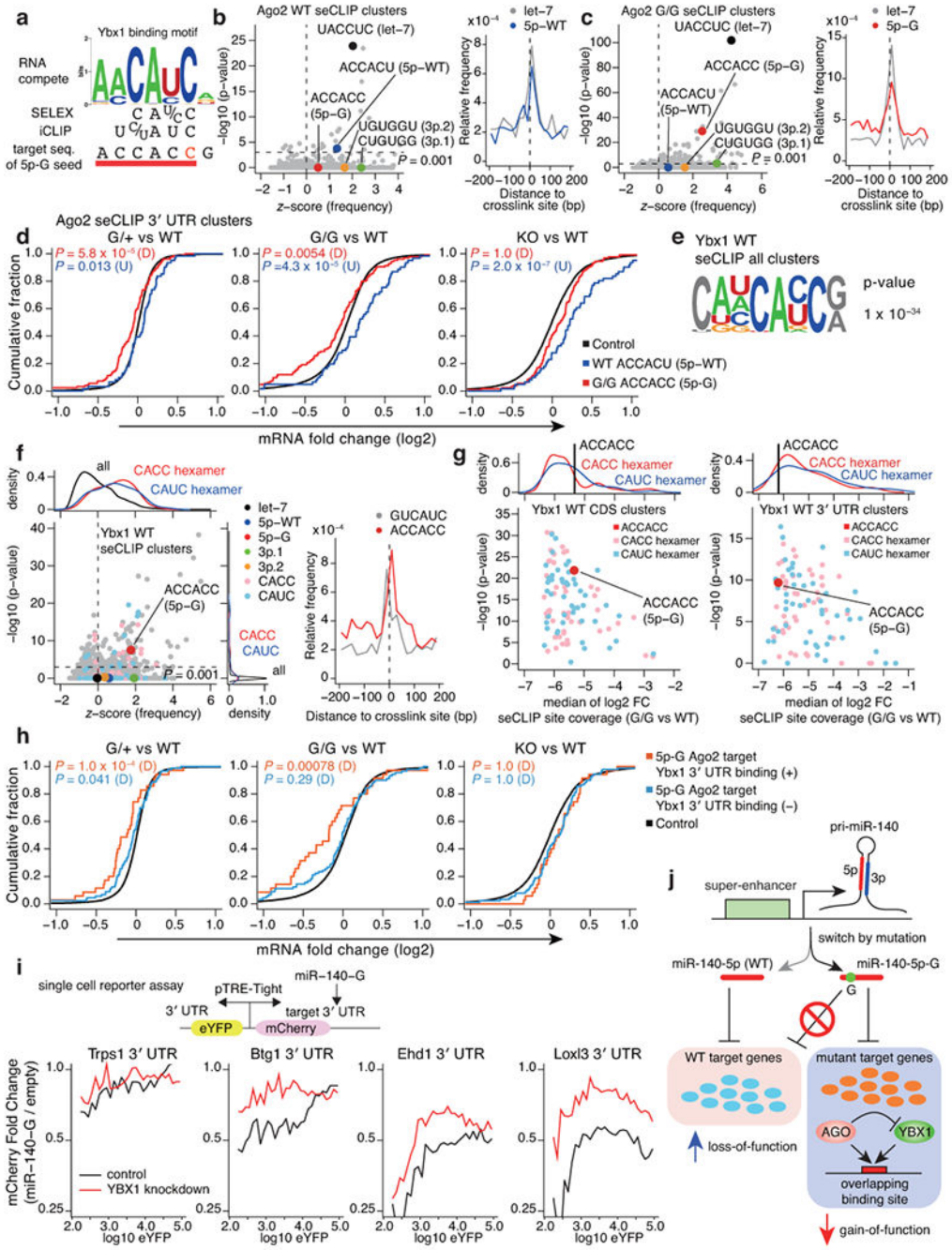

Figure 4. Competition between miR-140-5p-G and Ybx1

a, Overlap between previously reported Ybx1-binding motifs and complementary sequence of miR-140-5p-G seed region.

b, c, Hexamer enrichment analysis in non-intronic Ago2-bound seCLIP clusters identified in wild-type (**b**) and mutant (**c**) chondrocytes (WT, n = 4469 clusters; G/G, n = 6663 clusters). The *x* axis shows the z-scores of hexamer frequency. The *y* axis shows the negative log10 P value of two-sided Fisher's exact test with Bonferroni correction of the hexamer enrichment

above background. Right panels show the positional enrichment of indicated motifs around the crosslink site.

d, Cumulative distributions of fold changes of mRNAs with Ago2-bound seCLIP 3′ UTR clusters with ACCACC motif in mutant chondrocytes (red) or Ago2-bound seCLIP 3′ UTR clusters with ACCACU motif in wild-type chondrocytes (blue). P values (versus a control gene set) were calculated by one-sided Kolmogorov–Smirnov (K-S) test for either direction: upregulation (U) or downregulation (D) with Bonferroni correction (Control genes, n = 9428; miR-140-5p-WT, n = 61; miR-140-5p-G, n = 125).

e, A representative motif enriched in all Ybx1-bound seCLIP clusters in wild-type chondrocytes (n = 8354). Statistical analysis was performed using HOMER.

f, Hexamer enrichment analysis in non-intronic Ybx1-bound seCLIP clusters identified in wild-type chondrocytes (n = 5202). The graphs were plotted as in Fig. 4b.

g, Comparison of seCLIP signals at Ybx1-bound CDS seCLIP clusters (left, n = 2537) and Ybx1-bound 3′ UTR seCLIP clusters (right, n = 1649) containing individual CAUC or CACC motif, identified in wild-type chondrocytes, between the miR-140$^{G/G}$ and wild-type chondrocytes. The *x* axis shows the median of log2 fold changes of seCLIP signals between mutant and wild-type samples. The *y* axis shows the negative log10 P value of two-sided Wilcoxon rank sum test with Bonferroni correction.

h, Cumulative distributions of fold changes of expression levels of miR-140-5p-G target genes, identified by the Ago2 seCLIP, with or without Ybx1 binding in the 3′ UTRs (Control genes, n = 9428; miR-140-5p-G seCLIP target genes with Ybx1 binding, n = 35; miR-140-5p-G seCLIP target genes without Ybx1 binding, n = 90). Graphs are drawn as in Fig. 4d.

i, Single-cell 3′ UTR reporter assay in HEK293T cells transfected with Ybx siRNA, eYFP and mCherry dual reporter, and pri-miRNA expression plasmids. Fold changes of mean mCherry signal by miR-140-G overexpression across eYFP signal bins are shown. Suppressive effects by miR-140-G were dampened by Ybx1 knockdown.

j, Summary of the present study.